Three dimensional instability of the von Karman vortex street past a permeable circular cylinder: two-dimensional flow and DMD-based secondary stability analysis

6 authors, including:

Filippo Caruso Lombardi

Gran Sasso Science Institute

1 PUBLICATION **0** CITATIONS

SEE PROFILE

Alessandro Bongarzone

École Polytechnique Fédérale de Lausanne

15 PUBLICATIONS **33** CITATIONS

SEE PROFILE

Francois Gallaire

École Polytechnique Fédérale de Lausanne

237 PUBLICATIONS **5,194** CITATIONS

SEE PROFILE

Simone Camarri

Università di Pisa

90 PUBLICATIONS **1,506** CITATIONS

SEE PROFILE

Some of the authors of this publication are also working on these related projects:

Project Sensitivity and Stability Analysis View project

Von Karman vortex street past a permeable circular cylinder: two-dimensional flow and DMD-based secondary stability analysis

F. Caruso Lombardi[1,2], A. Bongarzone[1], G.A. Zampogna[1], F. Gallaire[1], S. Camarri[2], P.G. Ledda[3,1]*

[1]*Laboratory of Fluid Mechanics and Instabilities, École Polytechnique Fédérale de Lausanne, Lausanne, CH-1015, Switzerland*
[2]*Dipartimento di Ingegneria Civile e Industriale, Università di Pisa, 56122 Pisa, Italy,*
[3]*Dipartimento di Ingegneria Civile, Ambientale e Architettura,*
Università degli Studi di Cagliari, 09123 Cagliari, Italy

We investigate the wake structure and the three-dimensional stability of the two-dimensional von Kármán vortex street developing in the wake of a permeable circular cylinder. The flow through the porous medium, assumed homogenous and isotropic, is described by the Darcy law, with a Navier slip coupling condition at the interface with the pure fluid region. The two-dimensional and steady flow past the cylinder is initially considered. Permeability induces a downstream displacement of the recirculation region, which reduces its dimensions until it eventually disappears. Linear stability analysis shows that the flow is progressively stabilized as permeability increases. We identify a critical value of permeability beyond which the steady wake is linearly stable independently of the Reynolds number. Two-dimensional, time-dependent simulations are then carried out. A progressive downstream displacement of the region of onset of the vortex shedding is observed, together with a decrease of the oscillation frequency. Oscillations of aerodynamic forces are progressively quenched with permeability owing to the downstream displacement of the onset region of the vortex shedding. At the same time, traveling vortices are observed far downstream of the body, in opposition with the impervious case, characterized instead by the formation of two shear layers of opposite vorticity, at very large distances from the body. We perform linearized simulations for the evolution of three-dimensional perturbations on the two-dimensional von Karman vortex street. The growth rate and the spatial structure of the perturbations are extracted from such linearized dynamics by employing a Sparsity-Promoting Dynamic Mode Decomposition (SP-DMD). As permeability increases, the unsteady vortex street past the cylinder is progressively stabilized with respect to three-dimensional perturbations until the transition to three-dimensionality is prevented. We identify a critical value of the permeability beyond which the vortex shedding preserves its two-dimensionality, at least in the considered parameters space.

I. INTRODUCTION

The interaction between fluid flows and slender bluff bodies is a classical and relevant topic in fluid mechanics. Typical examples in civil and marine engineering are vibrations of pipelines lying on the seabed, interaction of currents and waves with off-shore structures in ocean engineering, skyscrapers, chimney stacks and suspension bridges [1]. These slender structures are often subject to an alternate shedding of vortices in the near wake, so-called von Karman vortex street, which may lead to large fluctuating forces on the body along both the flow direction and transversal one and may cause structural vibrations, acoustic noise, or resonance, with possible structural failure of the structures subject to these oscillating forces (cf. Williamson [2] and references therein for a review). Several studies focused on the problem of reducing the coherence of vortex shedding along the spanwise direction, often through surface modifications, e.g. appendages or helical cables [3, 4], thus reducing oscillating forces. However, Vortex Induced Vibrations (VIV) can also be advantageously used for energy harvesting [5, 6]. Recently, also microelectromechanical (MEMS) wind-energy harvesters composed of small cylindrical oscillators attached to piezoelectric MEMS devices have been proposed as a potential means of powering small off-grid sensors in a cost-effective manner due to the easy integration of the energy harvester and sensor on the same silicon chip [7]. As concerns environmental flows, deep-sea glass sponges (*E. aspergillum*) are tall, permeable, cylindrical shells anchored to the seabed that extend through the benthic boundary layer, composed of amorphous hydrated silica arranged in a highly regular and hierarchical structure. These sponges provide a natural shelter for a family of shrimps which feed themselves through the nutrients in suspension in the benthic boundary layer. The skeleton of *E. aspergillum* is characterized by exceptional structural properties, combined with remarkable hydrodynamic properties induced by their permeable structure, e.g. reduction of hydrodynamic stresses and the support of coherent internal recirculation patterns at low flow velocity [8].

The latter example shows how permeable structures offer an efficient way to maximize the structural and hydrodynamic performance of a particular flow configuration [9]. Permeability of the body can be achieved through active blowing systems, where a fixed velocity is imposed at the boundary [10], or in a passive way, e.g. exploiting the flow modifications induced by a microscopic structure [9]. Nature is always an invaluable source of inspiration when new technical solutions for optimal performances are needed. Dandelion seeds are spread by wind thanks to a bundle of radially oriented fibers, called pappus. Cummins et al. [11] showed the presence of a recirculation region that, instead of being attached to the rear of the object as

*Corresponding Author e-mail: piergiuseppe.ledda@unica.it

in the impervious case, moves downstream of the body. This wake configuration acts like a parachute and makes it arguably possible for the seeds to travel for long distances under the effect of light breezes. Similar studies on idealized permeable disks mimicking the dandelion pappus showed similar flow patterns [12], associated with hydrodynamic stability of the wake in the range of permeability and Reynolds numbers typical of dandelions [13]. The introduction of permeability thus offers interesting perspectives on flow control of wakes past bluff bodies. A documented study can be traced back to Castro [14], who studied the flow past a perforated flat plate, for Reynolds numbers of the order of 10^4. In the considered cases, the flow exhibited a vortex shedding, whose mean recirculation region was detached from the body. Also, Castro observed a decrease of the drag exerted on the porous plate. A similar detachment was analytically predicted by Steiros *et al.* [15], for perforated plates. A theoretical analysis on the drag exerted by perforated plates in free-flows with $Re \sim 1000$ was performed by Steiros & Hultmark [16], who showed a similar decreasing trend of the drag. The distribution of pores may also influence the aerodynamic forces [15]. The drag behavior with permeability was also analyzed in the creeping flow regime by Strong *et al.* [17]. Other investigations include also the effect of the fluid–structure interaction such as flexibility of porous strips [18]. The detachment of the mean recirculation region is associated with a downstream displacement of the vortex shedding onset, as shown by recent experimental [19] and numerical [20] studies. Ledda et al. [21] highlighted a similar effect on the steady flow at low Reynolds numbers past thick flat plates, characterized by the detachment and shrinking of the recirculation region as permeability was increased, until disappearance of the counterflow. A critical permeability threshold was identified, beyond which the onset of von Karman vortex street was prevented, regardless of the considered Reynolds number. Similar behaviors were observed in the case of permeable disks [12, 22], spheres [23, 24] and circular cylinders [25]. In the latter paper, the authors studied the two-dimensional, steady, flow past a circular permeable cylinder, showing the emergence of a detached recirculation region at low Reynolds numbers.

In the impervious case, it is well known that the steady flow past a circular cylinder undergoes a Hopf bifurcation at $Re = 46.7$, which leads to the previously-mentioned periodic shedding of vortices [26, 27]. The periodic unsteady wake remains two-dimensional until $Re \approx 190$, beyond which the vortex shedding becomes three-dimensional, while preserving a strong two-dimensional coherence [28, 29]. This *secondary* instability of the wake has been studied both experimentally [30–32] and theoretically [28, 29, 33]. Floquet stability analysis stems from the linearization of the flow equations around a time-periodic baseflow. The stability of the system can be inferred by studying the eigenvalues of the so-called monodromy operator, which maps the solutions from one period to the successive one [34]. The transition to a three dimensional flow is characterized by two different linear modes distinguished respectively by a long (mode A, at $Re \approx 190$) and short (mode B, at $Re \approx 260$) wavelength in the spanwise direction [35]. Barkley & Henderson [33] numerically confirmed the experimental observations made by Williamson [35] via a linear Floquet stability analysis on the two-dimensional, periodic, baseflow. The authors identified mode A as the leading mode for the three-dimensional transition of the von Karman vortex street past a circular cylinder. In these bluff body wakes [36], the physical mechanism originating in the development of mode A (the wavelength of which scales with the vortex core size) has been associated with the so-called elliptic instability ([37, 38] and [39] for a review), while mode B, which develops at a higher Reynolds number and has a shorter wavelength, was shown to result from the hyperbolic instability [40]. In contrast, for slender body wakes, two competing modes of opposite symmetry dominate with comparable growth-rates and wavelengths and they can both be unambiguously and quantitatively attributed to the elliptic instability [41]. The growth rate of the elliptic instability is proportional to the strain rate at the point of maximum vorticity, which is linked to the intensity of the deformation of the vortex cores.

However, rather than directly evaluating the eigenvalues of the monodromy matrix, Floquet analysis is often performed by time-marching of the linearized equations for several periods, combining it with iterative Arnoldi-like methods [33]. Such methods are based on an approximation of the high-dimensional system matrix by projecting it onto a lower-dimensional Krylov subspace, hence allowing a rather efficient extraction of the dominant eigenvalues. Data-driven techniques like Dynamic Mode Decomposition (DMD) have gained attention for their ability to extract dynamic flow features from experimental or numerical data [42–47]. The DMD algorithm allows for the data sequence to be approximated as a Krylov sequence. However, if the dynamics is produced by a linear process, there is no approximation and the DMD eigenmodes and eigenvalues at convergence are equivalent to those computed by a global stability analysis via Arnoldi-like methods based on a Krylov subspace [42]. In our framework, the snapshot sequence is produced by the linear flow evolution of small perturbations around a T-periodic base-flow, with T the oscillation period. In such a scenario, Floquet and DMD modes can be directly linked with each other [48], hence suggesting DMD as an alternative to more classical Floquet stability analysis tools. In this work, DMD will be employed to characterize the three-dimensional secondary instability of the flow past a permeable circular cylinder.

The objective of this paper is to explore the three-dimensional stability and transition scenarios in the wake past porous circular cylinders. In particular, the yet unexplored role of permeability in modifying the two-dimensional von Karman vortex and its three dimensional stability properties is investigated. The selected flow configuration, i.e. the flow past a circular cylinder, is prototypical for bluff body wakes, and the transition scenario has been largely investigated in the literature for the impervious case. To this purpose, the first choice concerns the method employed to describe the flow through the porous microstructure. Direct simulations of the flow around and within the permeable matrix are cost challenging due to the large range of length scales that characterize the flow dynamics through porous bodies [8, 49, 50] and potentially limited by the choice of a specific microscopic configuration. Techniques based on multiscale expansions and averaging techniques (*homogenization*, cf. [51]) can
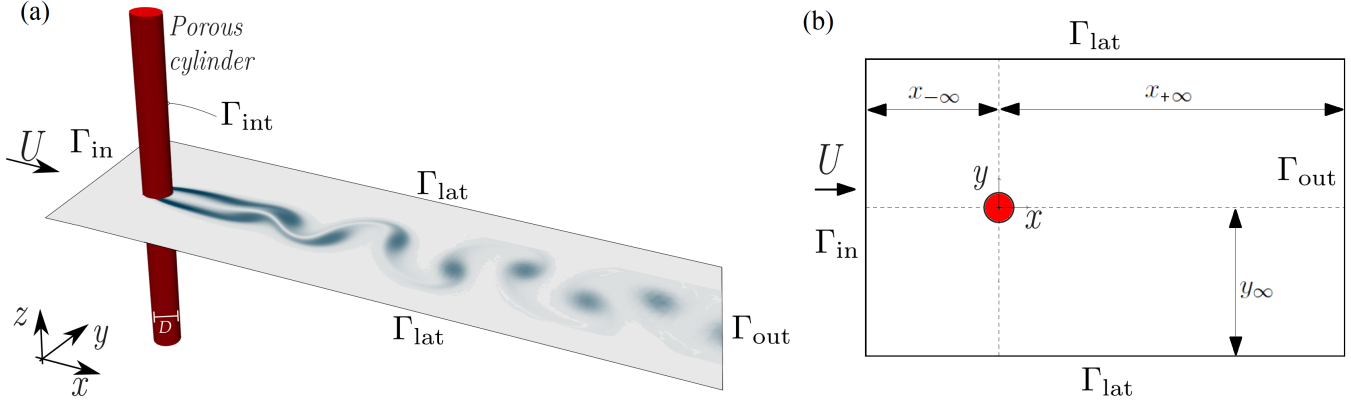
FIG. 1. Sketch of (a) flow configuration and (b) computational domain.

[111] reduce computational costs related to these multiscale problems by taking advantage of scales separation that is present in the
[112] dynamics of a fluid phase through a solid matrix. Homogenized models effectively recover the effects of the permeability on the
[113] whole fluid phase in terms of averaged variables, both in the case of thin [9, 52, 53] and thick [54–56] permeable objects, or when
[114] treating slip on a rough wall [57–59] or at the interface between a porous object and a free fluid region [60, 61]. Homogenization
[115] techniques have the great advantage to provide a rigorous framework that links the microstructure to macroscopic properties
[116] [62]. Therefore, the homogenized model does not suffer from the limitations stemming from the choice of a particular geometry.
[117] The calculations can be performed by employing macroscopic quantities (e.g. permeability), and the microscopic structure
[118] reproducing a certain macroscopic flow can be retrieved *a posteriori* through an inverse procedure [9, 24].
[119] In the introduced general framework, the investigation of the role of permeability in modifying the unsteady two-dimensional
[120] wake and the emergence of three-dimensional patterns is a crucial step forward in the understanding of large Reynolds number
[121] behavior of flows past permeable bluff bodies and the consequent three-dimensional fluid-structure interaction. The paper is
[122] organized as follows. Section II presents the mathematical formulation and numerical approach for the flow past and through a
[123] permeable circular cylinder. Section III is devoted to the study of the two-dimensional flow structure. We first identify the yet
[124] unknown linear stability boundary of the steady wake, and we then investigate the vortex shedding as permeability and Reynolds
[125] number of the flow are varied. Section IV studies, through a DMD-based algorithm, the three-dimensional stability of the two-
[126] dimensional vortex street, identifying the unstable modes and the boundary within which the two-dimensional solution is stable
[127] with respect to 3D perturbations.

II. PROBLEM FORMULATION AND NUMERICAL APPROACH

[129] In this section, we introduce the equations governing the problem as well as their numerical implementation. A permeable
[130] circular cylinder of diameter D is invested by a uniform free-stream of an incompressible Newtonian fluid with velocity U_∞ and
[131] kinematic viscosity ν, as shown in figure 1. The flow equations are solved in a Cartesian reference frame $(\bar{x}, \bar{y}, \bar{z})$, with the origin
[132] on the cylinder axis, which is parallel to the z direction as show in figure 1. We denote with $(\bar{\mathbf{u}}, \bar{p})$ and $(\bar{\mathbf{u}}_i, \bar{p}_i)$ the velocity and
[133] pressure field outside and inside of the cylinder, respectively. The flow equations are non-dimensionalized with the free-stream
[134] velocity and with the cylinder diameter. Dropping bars for non-dimensional variables, the Navier Stokes equations in the fluid
[135] region Ω_f outside the cylinder read:

$$\nabla \cdot \mathbf{u} = 0, \quad \frac{\partial \mathbf{u}}{\partial t} + \mathbf{u} \cdot \nabla \mathbf{u} + \nabla p - \frac{1}{Re} \nabla^2 \mathbf{u} = \mathbf{0}, \tag{1}$$

[136] where $Re = (UD)/\nu$ is the Reynolds number. The flow in the porous cylinder Ω_p is governed by the Darcy Law [54]

$$\mathbf{u}_i = -Re\mathbf{Da}\nabla p_i, \quad \nabla \cdot \mathbf{u}_i = 0 \tag{2}$$

[137] coupled with the following slip condition at the interface Γ_{int} [61–64]:

$$\mathbf{u}|_{\Gamma_{\text{int}}} - \left(-Re\mathbf{Da}_{\text{int}}\nabla p_i|_{\Gamma_{\text{int}}}\right) = \mathbf{\Lambda}\left(\Sigma(\mathbf{u}, p)|_{\Gamma_{\text{int}}}\mathbf{n}\right), \quad p_i|_{\Gamma_{\text{int}}} = -\mathbf{n} \cdot \left(\Sigma(\mathbf{u}, p)|_{\Gamma_{\text{int}}}\mathbf{n}\right), \tag{3}$$

[138] where Λ is the slip tensor (to be defined later), $\Sigma(\mathbf{u}, p) = -p\mathbf{I} + \frac{1}{Re}\left(\nabla\mathbf{u} + \nabla\mathbf{u}^T\right)$ is the non-dimensional stress tensor of the
[139] external flow, $\mathbf{Da} = \frac{\boldsymbol{\kappa}}{D^2}$ and $\mathbf{Da}_{\text{int}} = \frac{\boldsymbol{\kappa}_{\text{int}}}{D^2}$ are respectively the Darcy tensor evaluated in the bulk and at the interface, i.e. the

non-dimensional versions of the bulk and interface permeability tensors $\boldsymbol{\kappa}$ and $\boldsymbol{\kappa}_{\text{int}}$. The macroscopic flow problem is closed by the far-field boundary conditions in the fluid domain, i.e. a uniform free stream condition $\mathbf{u} = \mathbf{e}_x$ at the inlet Γ_{in} and a zero-stress condition $\Sigma(\mathbf{u}, p)\mathbf{n} = \mathbf{0}$ on the lateral and downstream boundary Γ_{out}.

The interface condition relies on a discontinuity of the velocity field related to the slip tensor $\boldsymbol{\Lambda} = \frac{\bar{\boldsymbol{\Lambda}}}{D}$. When represented in cylindrical coordinates, the tensor is diagonal, with non-zero components denoted with Λ_t and Λ_s, where $\mathbf{t}$ and $\mathbf{s}$ are the tangential vectors to the cylindrical interface. The slip tensor thus reads

$$\boldsymbol{\Lambda} = \Lambda_t \mathbf{t} \otimes \mathbf{t} + \Lambda_s \mathbf{s} \otimes \mathbf{s}, \tag{4}$$

where $(\mathbf{a} \otimes \mathbf{b})_{ij} = a_i b_j$ [57]. Depending on the considered values of permeability and slip, different microscopic configurations can be described. The imposition of zero permeability and a non-zero slip represents the case of a rough wall, which is described through a classical Navier slip condition [57–59]. A slip velocity, in the generic case, models the viscous effects in the vicinity of the interface, where the flow passes from the free-stream value to the one imposed by the Darcy law. The imposition of zero slip thus neglects viscous terms in the vicinity of the interface and gives the continuity of fluid stresses.

In analogy with Ciuti et al. [24], the numerical implementation of the Darcy law is based on a second-order PDE for p_i:

$$\nabla \cdot \mathbf{u}_i = -Re \nabla \cdot (\mathbf{Da} \nabla p_i) = 0 \Rightarrow \nabla \cdot \nabla (\mathbf{Da} p_i) = 0. \tag{5}$$

The free-fluid and porous problems are coupled via a domain decomposition method [65]. We exploit the finite element software COMSOL Multiphysics for the numerical implementation. The numerical method relies on the weak form of equations (1,2), together with their boundary conditions, where $P2 - P1$ Taylor-Hood elements for the fluid domain are employed, whereas the inner pressure p_i is discretized through $P1$ elements. The numerical tolerance is set to 10^{-6}, for all problems considered in this work. The steady problem and the stability analysis are solved via the built-in Newton algorithm and eigenvalue solver, the latter based on the ARPACK library. We employ a second-order Backward Differentiation Formula solver for the numerical solution of time-dependent problems. The results of the convergence analysis in terms of domain size and discretization, for the various problems considered here, are reported in Appendix A.

While representing the macroscopic effect of an actual microscopic structure, the permeability, interfacial permeability and slip are treated as free parameters. This approach ensures that the presented results are independent of the considered microscopic geometry. The aim of this work is to give a general picture of the flow past an isotropic and homogenous permeable circular cylinder, i.e. we consider $\mathbf{Da} = Da\mathbf{I}$. Since the bulk and interface permeability typically scale in the same way, i.e. $Da \sim Da_{\text{int}}$ [24], here we assume $\mathbf{Da}_{\text{int}} = \mathbf{Da} = Da\mathbf{I}$. Following Beavers and Joseph [66], the permeability and slip properties are not independent since they stem from the same microscopic geometry. In the following, we impose the classical scaling which relates permeability and slip, i.e. $\Lambda_t \sim \Lambda_s \sim \sqrt{Da}$. In the following, we thus assume $\Lambda_t = \Lambda_s = \sqrt{Da}$.

III. TWO-DIMENSIONAL FLOW

In this section, we characterize the two-dimensional flow past a permeable circular cylinder for $Re < 200$. We first study the steady solution of the problem and we identify the boundaries in which this solution is linearly stable through linear stability analysis. We then study the time-dependent solution emerging beyond these boundaries. The numerical results presented in this section are obtained using the mesh M4, details of which are given in Table I.

A. Steady flow

In this section, we consider the steady two-dimensional solution of the flow equations and its stability with respect to two-dimensional, time-dependent, perturbations. The steady solution of the equations $(\mathbf{U}, P, \mathbf{U}_i, P_i)$, with $\mathbf{U} = (U_x, U_y)$ and $\mathbf{U}_i = (U_{ix}, U_{iy})$ is given by

$$\nabla \cdot \mathbf{U} = 0, \quad \mathbf{U} \cdot \nabla \mathbf{U} + \nabla P - \frac{1}{Re} \nabla^2 \mathbf{U} = \mathbf{0}, \quad \nabla^2 P_i = 0, \tag{6}$$

together with the boundary conditions at the cylinder interface

$$\mathbf{U}|_{\Gamma_{\text{int}}} - \left(-Re Da \nabla P_i|_{\Gamma_{\text{int}}}\right) = \sqrt{Da} \Sigma(\mathbf{U}, P)|_{\Gamma_{\text{int}}} \mathbf{n}, \quad P_i = -\mathbf{n} \cdot \left(\Sigma(\mathbf{U}, P)|_{\Gamma_{\text{int}}} \mathbf{n}\right). \tag{7}$$

The problem is completed with the inlet free-stream $\mathbf{U} = \mathbf{e}_x$ and free-stress $\Sigma(\mathbf{U}, P)\mathbf{n} = \mathbf{0}$ conditions at the outlet [67] and lateral boundaries. The latter condition is equivalent to a free-slip as long as the free-stream flow at the sides of the domain are not influenced by the presence of the body, i.e. the blockage is negligible (see Appendix A).
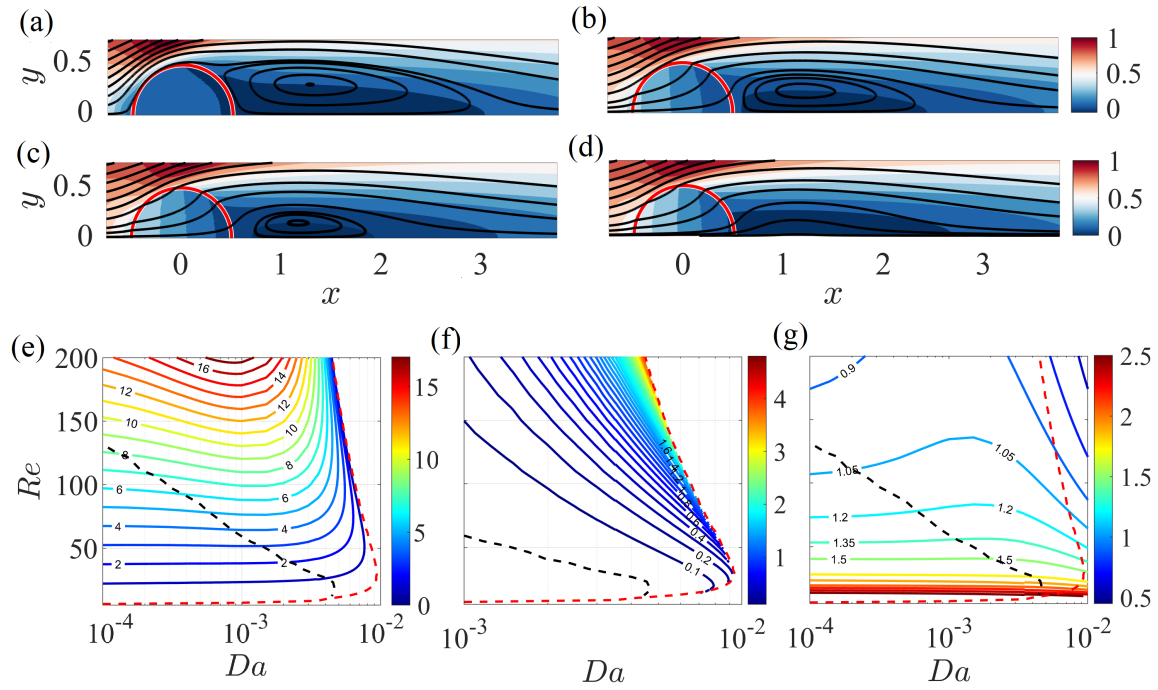
FIG. 2. Steady flow streamlines and iso-contours of the streamwise component of the velocity field for $Re = 45$ and (a) $Da = 10^{-4}$, (b) $Da = 5 \times 10^{-3}$, (c) $Da = 7 \times 10^{-3}$, (d) $Da = 9 \times 10^{-3}$. Note that only the region $y > 0$ is reported, because of symmetry. (e, f, g) Isocontours (e) of the length of the recirculation region L_R, (f) of the distance between the recirculation region and the cylinder X_R and (g) of the drag coefficient. The red and black dashed lines denote the zero iso-contours of L_R and X_R, respectively.

Figure 2(a-d) shows the steady flow streamlines past an increasingly permeable circular cylinder, for fixed $Re = 45$. While at low permeability $Da = 10^{-4}$ the flow features are analogous to the solid case, at $Da = 5 \times 10^{-3}$ a slightly smaller recirculation region, detached from the body, is observed. As permeability further increases, the recirculation region moves away from the cylinder, becomes smaller and disappears. Even in the absence of a recirculation region (subfigure (d)), there is a region of very low velocity downstream of the cylinder. The behavior of the recirculation region is summarized in figure 2(e-f), which shows the iso-contours of its length L_R (i.e. the streamwise distance between the two points on the axis $y = 0$ on which the streamwise velocity is identically zero) and its distance from the rear of the cylinder X_R (i.e. the distance x from the rear of the cylinder at which the streamwise velocity becomes negative). At low Reynolds numbers, an increase in Da leads to a decrease of L_R. However, for large enough Re, the length of the recirculation region shows an initial increase with Da followed by a decrease, until it disappears. For $Da > 0.004$, L_R presents a non-monotonous behavior for increasing Re, with an initial increase followed by a rapid decrease, until disappearance of the recirculation region. The distance of the recirculation region increases with the permeability and reaches very large values, of the order of ≈ 4 diameters at large Reynolds numbers.

In analogy with other permeable bodies studied in the literature [9, 13, 21, 24], the two-dimensional steady flow past a permeable cylinder presents a detached recirculation region. In general, the recirculation region shrinks and disappears as Da increases. The shrinking and detachment of the recirculation region stem from the intensity of vortical layers generated by the flow separation. An increase in permeability leads to larger velocities through the body and to a less perturbed flow, with respect to the free-stream condition. Therefore, the strength of vortical layers induced by flow separation is reduced, leading to a lower counterflow and smaller recirculation regions. This effect is combined with the presence of a positive bleeding flow through the cylinder which leads to a downstream displacement of the recirculation. The non-monotonous behavior of the length of the recirculation region with increasing Re is related to the competition between the increase of the flow inertia (which tends to increase L_R), in analogy with what happens in the case of impervious bodies, and the decrease of the microscopic viscous drag $\boldsymbol{u}/(ReDa)$ $1/Re$ exerted by the porous structure (which tends to decrease L_R), since the velocity through the pores increases with Re (see equation (2)) [9].

The modifications of the flow morphology also affect the behavior of the drag coefficient $C_D = 2 \int_{\Gamma_{\text{int}}} \Sigma(\mathbf{U}, P) \mathbf{n} \cdot \mathbf{e}_x d\Gamma$ The drag coefficient monotonically decreases at low Reynolds numbers. However, for $Re > 100$, a clear peak in the iso-contours is visible, thus highlighting a non-monotonous behavior with permeability. This behavior is analogous to the one of L_R, since both are related to the intensity of vorticity in the field, which in turn relates to the microscopic drag at the pore scale.

These analyses have been performed by considering the steady solution of the flow equations. However, not all described flow configurations are likely to be observed, since the steady wake may be unstable to perturbations. In the solid case, the wake

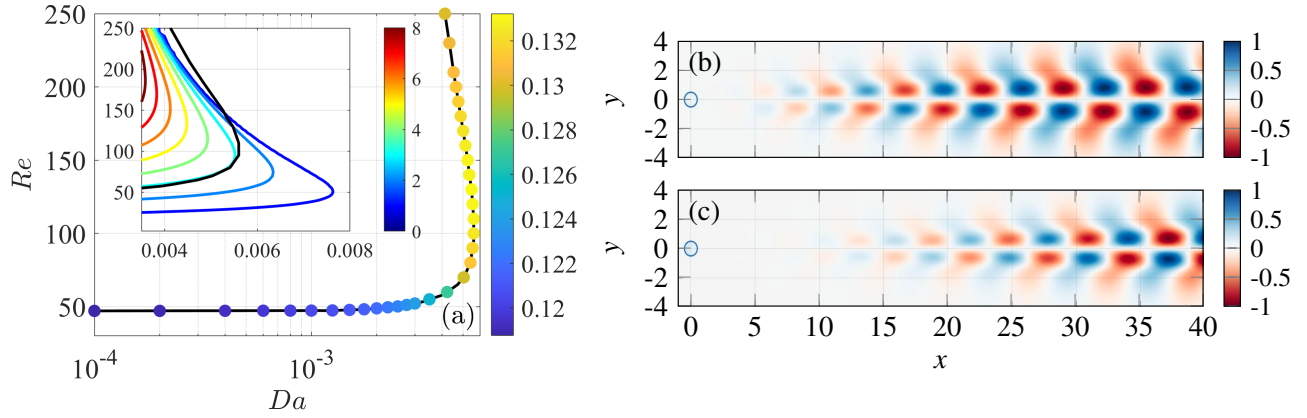FIG. 3. (a) Neutral curve in the (Da, Re) plane, together with the values of St following the marginal stability (colored dots). In the inset: zoom in the region $0.0035 < Da < 0.008$ (black solid line), together with the iso-contours of the length of the recirculation region L_R. (b,c) Streamwise component of the velocity eigenmode at the marginal stability, for $Da = 5.032 \times 10^{-3}$ and (b) $Re = 85$, (c) $Re = 130$.

past a circular cylinder undergoes a Hopf bifurcation at $Re \approx 46.7$, leading to the well-known von Karman vortex street, i.e. an alternate shedding of vortices with a well-defined frequency [26]. Linear stability analysis can be used to identify the critical conditions which lead to the instability of the steady flow and the onset of an unsteady wake. Linear stability techniques rely on the introduction of the following decomposition in the flow equations (1) and (2), with $\varepsilon \ll 1$:

$$\mathbf{u}(x,y,t) = \mathbf{U}(x,y) + \varepsilon \mathbf{u}'(x,y,t), \quad p(x,y,t) = P(x,y) + \varepsilon p'(x,y,t), \quad p_i(x,y,t) = P_i(x,y) + \varepsilon p_i'(x,y,t). \tag{8a}$$

While at $\mathcal{O}(1)$ one recovers the steady equations satisfied by $(\mathbf{U}, P, P_i)$, a time-dependent linear problem is obtained at order $\mathcal{O}(\varepsilon)$. Upon introduction of a normal mode ansatz, i.e.

$$\left(\mathbf{u}'(x,y,t), p'(x,y,t), p_i'(x,y,t) \right) = (\hat{\mathbf{u}}(x,y), \hat{p}(x,y), \hat{p}_i(x,y)) \exp(\sigma t), \tag{9}$$

the following eigenvalue problem is obtained:

$$\nabla \cdot \hat{\mathbf{u}} = 0, \quad \sigma \hat{\mathbf{u}} + \mathbf{U} \cdot \nabla \hat{\mathbf{u}} + \hat{\mathbf{u}} \cdot \nabla \mathbf{U} + \nabla \hat{p} - \frac{1}{Re} \nabla^2 \hat{\mathbf{u}} = \mathbf{0}, \quad \nabla^2 \hat{p}_i = 0, \tag{10}$$

together with the interface condition

$$\hat{\mathbf{u}}|_{\Gamma_{\text{int}}} - \left(-ReDa \nabla \hat{p}_i|_{\Gamma_{\text{int}}} \right) = \sqrt{Da} \left(\Sigma(\hat{\mathbf{u}}, \hat{p})|_{\Gamma_{\text{int}}} \mathbf{n} \right), \quad \hat{p}_i|_{\Gamma_{\text{int}}} = -\mathbf{n} \cdot \Sigma(\hat{\mathbf{u}}, \hat{p})|_{\Gamma_{\text{int}}} \mathbf{n}, \tag{11}$$

completed with the homogenous condition $\hat{\mathbf{u}} = \mathbf{0}$ at the inlet and the stress-free condition $\Sigma(\hat{\mathbf{u}}, \hat{p})\mathbf{n} = \mathbf{0}$ on the lateral and outlet boundaries. The real and imaginary parts of the complex eigenvalue $\sigma = \text{Re}(\sigma) + i\text{Im}(\sigma)$ are the growth rate and oscillation frequency of the global mode. Modes with $\text{Re}(\sigma) > 0$ grow exponentially with time and are thus unstable. In this work, we identify the critical value of Re and Da for which $\text{Re}(\sigma) = 0$, together with the corresponding spatial distribution of the marginally stable mode. The grid convergence analysis of the eigenvalue problem is reported in Appendix A.

Figure 3(a) shows the marginal stability curve for the onset of the vortex shedding, i.e. the couples (Re, Da) for which the flow presents null growth rate. The marginal stability curve divides the parameters' space into a stable and unstable region. For $Da = 10^{-4}$, the critical Reynolds number for the marginal stability is analogous to the solid case, i.e. $Re_{cr} = 46.7$. As permeability increases, Re_{cr} remains constant until $Da = 10^{-3}$, beyond which it starts to increase. The marginal stability curve presents an inversion point for $Da \approx 6 \times 10^{-3}$. Close to this value, an increase of Re with constant Da leads to an initial destabilization, followed by a re-stabilization at larger Reynolds numbers. The non-dimensional frequency, expressed in terms of Strouhal number $St = \text{Im}(\sigma)/(2\pi)$, does not show strong variations with Da and Re, when considered along the marginal stability curve, even if a slight increase with Da is observed. In the inset of figure 3, the marginal stability curve is overlaid with the iso-contours of the length of the recirculation region. The marginal stability curve follows the iso-contour $L_R \approx 3$ before the inversion point. After the inversion point, the marginal stability curve crosses decreasing isolevels of L_R. For large enough Re, the neutral curve is located in a region where the recirculation region is absent.

The highlighted behavior of the marginal stability curve is analogous to the one observed for different shapes[24] and permeable models [9, 13, 21]. Since the neutral curves reasonably follow the iso-contours of the length of the recirculation region [21], the inversion point observed in figure 3 is due to the non-monotonous behavior of the recirculation region with Re, related
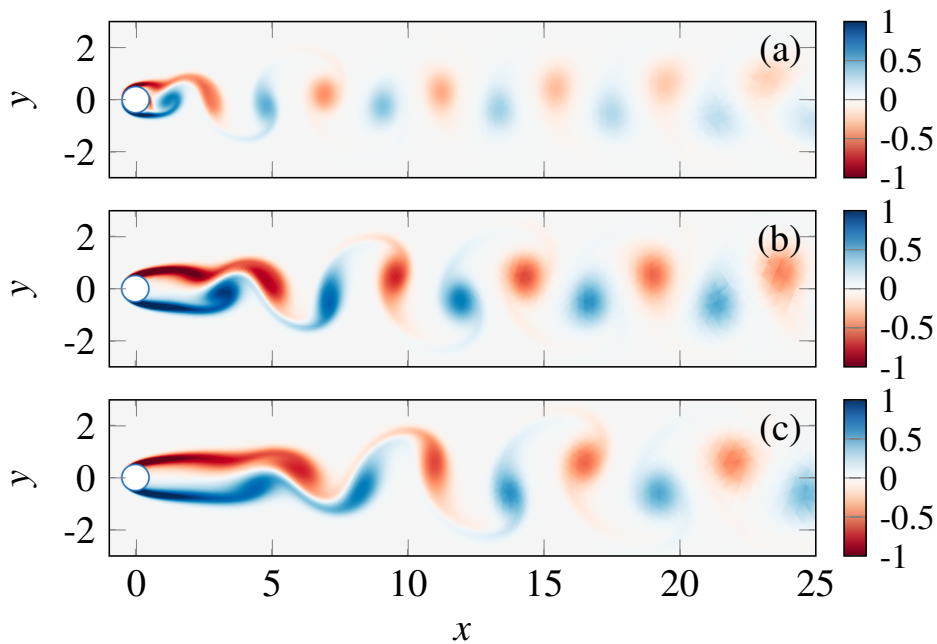
FIG. 4. Spanwise base-flow vorticity snapshots for (a) $Re = 215, Da = 1 \times 10^{-4}$, (b) $Re = 200, Da = 2 \times 10^{-3}$ and (c) $Re = 215, Da = 3 \times 10^{-3}$, normalized with the corresponding maximum absolute value, i.e. (a) $\max(|\omega_z|) = 27.3$, (b) $\max(|\omega_z|) = 8.3$, (c) $\max(|\omega_z|) = 6.1$.

236 to the competition between the flow inertia and the decrease of the drag through the pores. The presence of an unstable region
237 without recirculation was already highlighted in Ledda et al. [21]. Despite the absence of a recirculation region, there is a strong
238 wake defect past the cylinder (as shown in figure 2(d)) which is enough to trigger the oscillatory instability [68, 69].
239   The properties of the recirculation region also influence the spatial structure of the critical modes, shown in figure 3(b). We
240 consider two cases for fixed $Da \approx 5 \times 10^{-3}$ and increasing Re. The case $Re = 85$ shows a spatial distribution very similar to
241 the solid case, with a slight downstream displacement of the onset region of the vortex shedding. However, for $Re = 130$, the
242 onset region moves further downstream. While the length of the recirculation region L_R modifies the stability properties of the
243 wake, its distance from the cylinder X_R has a deep influence on the vortex-shedding onset region. The onset region is typically
244 related to the position of the instability, so-called wavemaker [69], that, with a good approximation, corresponds to where the
245 recirculation region or the wake defect is located [21, 69]. Therefore, the downstream displacement of the wake defect of the
246 steady flow moves downstream the vortex shedding onset location. This downstream displacement may have a profound impact
247 on the non-linear unsteady flow and in particular on the forces acting on the cylinder, analyzed in the next section.

B.   Two-dimensional von Karman vortex street

249   In the previous section, we characterized the steady flow and identified the boundaries in the (Da, Re) plane where this
250 solution can be observed. In this section, we cross this threshold in the parameters' space and consider the unsteady, non-linear
251 solution of the flow equations introduced in Section II. The numerical results presented in this section are obtained adopting a
252 mesh derived from mesh M4 (see Table I) with a reduced outflow length $L_{out} = 90$ according to results given in Table II. For
253 further details in terms of numerical convergence, we refer to Appendix A. The field is initialized with the initial condition
254 $u = (1, 0)$; the first 100 time units are discarded to let transient effects fade away and results are presented after a periodic
255 state (observed through the monitoring of aerodynamic forces) in the near wake is attained. Figure 4 presents typical vorticity
256 patterns observed by progressively increasing the cylinder permeability. For $Da = 10^{-4}$, the flow features are analogous to the
257 solid case, with vortices that are shed from the cylinder. However, for $Da = 2 \times 10^{-3}$, two shear layers of opposite vorticity are
258 observed just downstream of the body. At $x \approx 2$, the shear layers become unstable and vortices are shed in the wake, with larger
259 spacing between the vortical structures of opposite signs, compared to the previous case. A further increase in Da moves further
260 downstream the onset region, and the distance between vortical structures increases. In addition, the wavelength (and the period
261 as seen below) of the shedding increases with increasing Da.
262   The downstream displacement of the onset region induces a variation of the periodic aerodynamic forces exerted on the
263 cylinder. Figure 5(a) shows the variation with time of the drag coefficient, rescaled with its mean value in the plotted time range,
264 and of the lift coefficient C_L, for increasing values of Da and fixed $Re = 200$. In all cases, a well-defined oscillation frequency
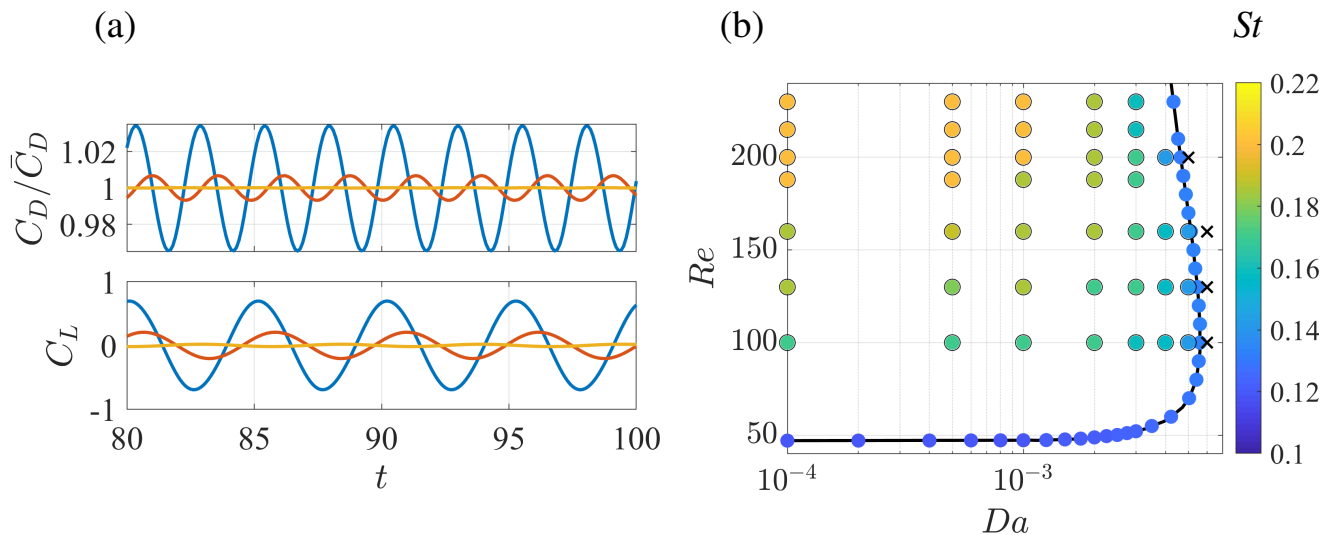
FIG. 5. (a) Drag coefficient rescaled with its mean value (on the top) and lift coefficient (on the bottom) as functions of time, for $Re = 200$ and $Da = 10^{-4}$ (blue), $Da = 10^{-3}$ (orange), $Da = 2 \times 10^{-3}$ (yellow). (b) Scatter plot in the (Re, Da) plane of the Strouhal number obtained from the DNS (colored dots in the black circles). The black solid line denotes the marginal stability curve while the colored dots on it the values of St obtained from the linear stability analysis. Crosses instead denote nonlinear simulations which converged to a steady solution.

is identified. In the almost-solid case, the oscillation frequency of the drag coefficient is twice the one of the lift coefficient, in agreement with the solid case [2]. For both quantities, the frequency slightly decreases as permeability increases. An increase of permeability also leads to a decrease of the amplitude of the oscillations of the drag coefficient with respect to its mean value. At the same time, the lift oscillations amplitude decreases. For $Da \approx 2 \times 10^{-3}$, the C_D oscillations are almost damped, while those of C_L are reduced by two orders of magnitude.

The presence of a well-defined frequency in the time history of the aerodynamic forces allows us to use them in evaluating the Strouhal number of the wake. In particular, we employ the lift coefficient, to this purpose. Figure 5(b) shows the values of St in the (Da, Re) plane, together with the values obtained from the linear stability analysis, which lie on the marginal stability curve. The crosses identify cases in which the non-linear time-dependent simulations lead to a steady flow. These results agree with the linear stability analysis of the previous section. Overall, St increases as Da and Re progressively depart from the marginal stability curve. At low permeability, an increase in the Reynolds number leads to a monotonic increase of St, from ≈ 0.1 to ≈ 0.22. For fixed Re, instead, the Strouhal number decreases with permeability. For $Da = 4 \times 10^{-3}$, a non-monotonous behavior of St with Re is observed, starting from the initial marginal stability at $Re \approx 60$ to the recovered neutral curve at $Re \approx 250$, in analogy with the behavior of recirculation region and drag coefficient.

The non-linear unsteady simulations show that the von Karman vortex street forms in a region which progressively moves downstream as permeability increases. This result, experimentally observed by [19] at larger Reynolds numbers, is in agreement with the spatial distribution of the linear stability modes and is related to the downstream displacement of the recirculation region. Since the onset of shedding can take place significantly downstream of the cylinder, the intensity of the flow oscillations in the vicinity of the cylinder decrease. As a consequence, the drag and lift oscillation amplitudes decrease, until an almost constant value of drag and a vanishing lift are reached, although vortex shedding is still present (see figure 5). The decrease of Strouhal number for increasing Da is indirectly visible in figure 4. The vortices present a larger spacing as permeability increases, for fixed Re. Therefore, the vortices are shed with a lower frequency since the advection velocity of these vortices, related to the free-stream velocity, is the same in all cases. An increase in permeability reduces the intensity of the separation since more fluid can pass through the body, reducing the adverse pressure gradients. Amplification of perturbations is thus reduced and the unstable region moves downstream, as shown by [21] with local stability analysis for a permeable rectangle. Therefore, perturbations grow to significant amplitude only further downstream from the cylinder, with a consequent frequency reduction. This analysis is confirmed by observing figure 4, in which the maximum value of vorticity decreases and shear layers destabilize further downstream as permeability increases. Permeability reduces the intensity of produced vorticity, with a consequent downstream displacement of vortex shedding onset region and a decrease of the shedding frequency, since perturbations need to be advected more downstream to be sufficiently amplified. These flow modifications damp and eventually suppress the oscillations of the aerodynamic forces acting on the cylinder.

Figure 6 shows the mean flow streamlines, obtained by averaging the time-dependent periodic flow over one period. In analogy with the steady case, the mean flow presents a recirculation region that detaches from the body and moves downstream as permeability increases. The behavior of the recirculation region of the mean flow in terms of length L_R and distance X_R is

299 summarized in figure 7(a,b). Its presents a non-monotonous behavior with Da, for fixed Re, with an initial increase followed by
300 a very steep decrease until disappearance of the recirculation. The maximum values reached are of the order of $L_R \approx 1 - 2$. The
301 distance instead always increases with Da, reaching a maximum value of ≈ 2.5, for the considered cases. These results are in
302 line with the experiments of Castro [14], where a detached mean recirculation region past a perforated plate was observed, at
303 Reynolds numbers of the order of 10^4. The presence of a detached recirculation region of the mean flow is thus a footprint of
304 the permeability of the bluff body penetrated by the flow, in addition to the behavior observed in the steady case.

305 The mean values of the drag coefficient and the maximum lift coefficient are reported in figure 7(c,d). The maximum lift
306 coefficient monotonically decreases with Da, reaching very small values (≈ 0.01) for $Da > 3 \times 10^{-3}$. The values of lift are
307 intrinsically related to the oscillations in the near wake. Since, as Da increases, the onset region of the vortex shedding is moved
308 downstream, oscillations of the lift coefficient decrease until they become negligible. Similarly, for large enough permeability,
309 no significant drag oscillations are observed. Interestingly, the mean drag coefficient presents a maximum for intermediate
310 permeability, in the vicinity of $Da \approx 10^{-3}$, beyond which it decreases monotonically. This maximum of drag is realized for
311 slightly lower values of permeability, when compared to the steady baseflow.

312 We conclude our analysis of the two-dimensional vortex shedding by showing the far-wake behavior of the von Karman
313 vortex street. Figure 8(a) shows the far wake distribution of the vorticity field, for $Da = 9 \times 10^{-4}$ and $Re = 195$. In analogy
314 with the solid case [70], the vortex street past the cylinder decays and two shear layers of opposite vorticity emerge. The shear
315 layers are known to be convectively unstable and amplify a broad band of frequencies [70]. However, an increase in Da (figure
316 8(b,c)) leads to a downstream displacement of the vortex shedding decay region, and vortices are observed for a much larger
317 downstream extent. The long distance behavior is related to the streamwise spacing of the vortices. In panel (a), vortices are less
318 spaced than in panel (c). As the spacing increases, vortices of opposite sign present a weaker interaction, and these structures
319 thus annihilate at larger distances from the cylinder. Since the shedding frequency decreases with increasing permeability, also
320 the spacing of vortices increases with permeability, which survive longer downstream. Therefore, when compared to impervious
321 obstacles, permeable bodies present a spatially-retarded emergence of the far-field shear layers associated to a longer region of
322 influence of the shedding extending further downstream. This observation is in agreement with the results of [21], where the
323 authors showed that the core of the instability (i.e. the wavemaker [69], see Section III A) extends several diameters downstream
324 of the body.

325 Another interesting flow feature appears in the far wake, at large times: the shear layers resulting from the annihilation of the
326 vortex street destabilize and vortical structures are advected downstream, which constitute the so-called *secondary vortex street*.
327 Mittal et al. [70] also observed, in the impervious case for a circular cylinder, that the vortical structures in the far wake region
328 lack of the periodicity typical of the near wake region and that the size of these structures grow as they are advected downstream.
329 A work carried out by Vorobieff et al. [71] confirmed such a flow pattern trough a PIV analysis of experimental data. Figure 9
330 shows the frequency spectra of the cross-stream component of the velocity for the flow case corresponding to $Da = 1 \times 10^{-4}$
331 and $Re = 188.5$ and $Da = 9 \times 10^{-4}$ and $Re = 240$ sampled at various streamwise locations. As described in [70], the near-wake
332 dominant frequency corresponds to the von Kármán shedding frequency (St_{VK}) and the flow locally is exactly periodic. Moving
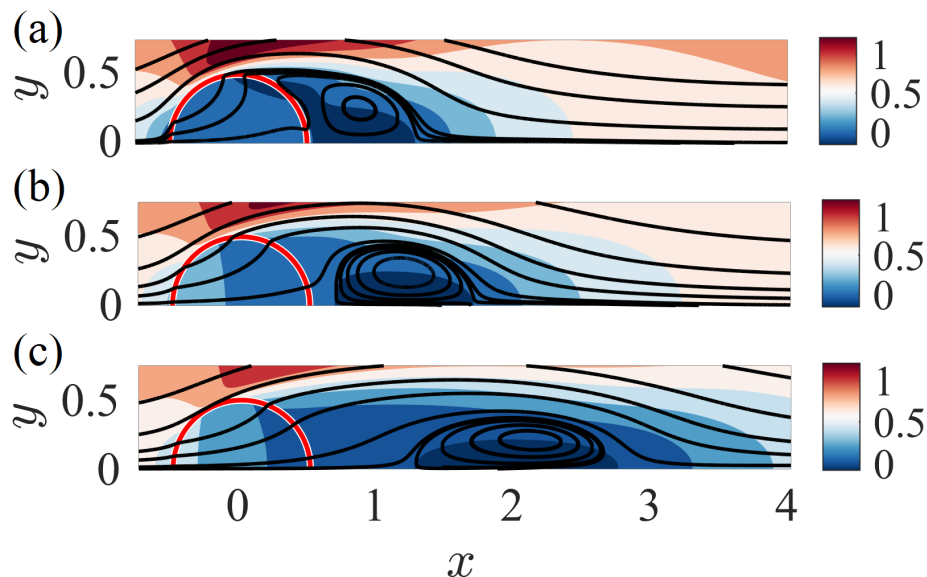

FIG. 6. Mean flow streamlines and iso-contours of the mean streamwise velocity for $Re = 200$ and (a) $Da = 10^{-4}$, (b) $Da = 10^{-3}$, (c) $Da = 2 \times 10^{-3}$.
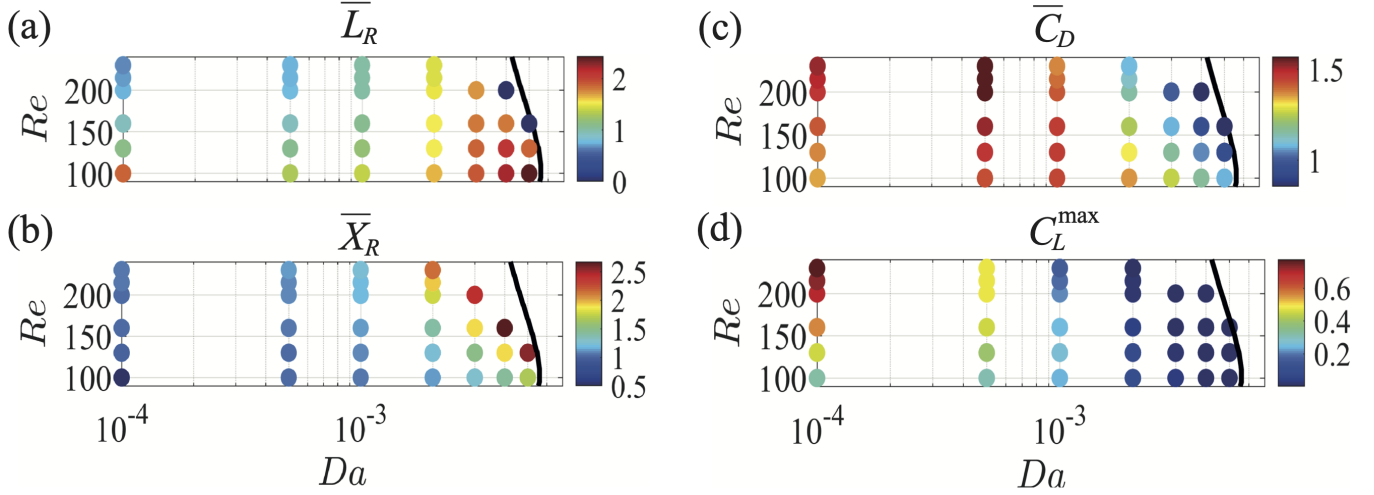
FIG. 7. (a) Length of the recirculation region of the mean flow $\bar{L}_R$ (on the top) and its distance from the cylinder $\bar{X}_R$ (on the bottom) in the (Da, Re) plane. (b) Mean drag $\bar{C}_D$ (on the top) and maximum lift $C_L^{\max}$ (on the bottom) coefficients in the (Da, Re) plane. The black line denotes the marginal stability curve.
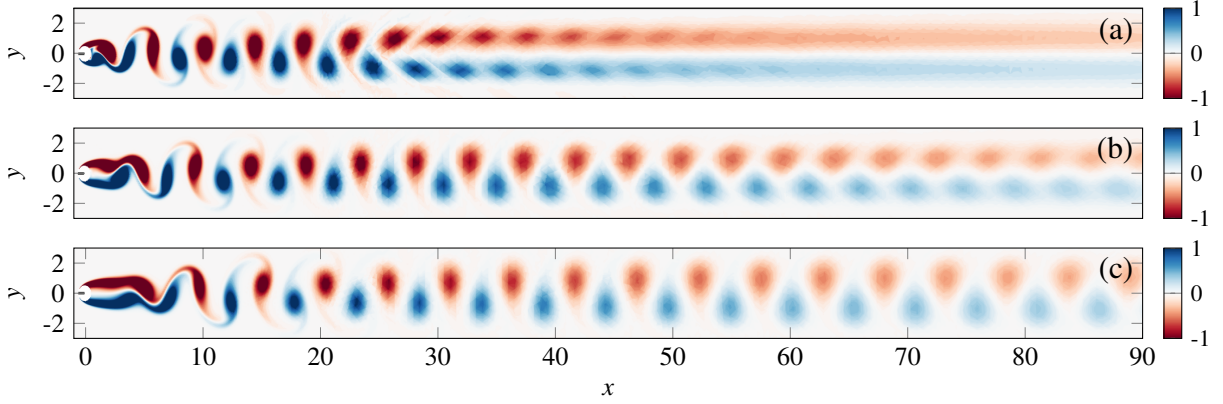

FIG. 8. Vorticity field (rescaled with the maximum absolute value) iso-contours at large times for (a) $Da = 9 \times 10^{-4}$, (b) $Da = 2 \times 10^{-3}$ and (c) $Da = 3 \times 10^{-3}$ for $Re = 200$ at a non-dimensional time $t = 180$.

downstream, the velocity spectra exhibit a gradual shift to broad-band frequencies centered around a frequency lower than f_{VK} for a wide range of parameters in the $Re - Da$ plane. Figure 10 shows the behavior of the far wake for the case $Re = 240$ and $Da = 9 \times 10^{-4}$. Although the near-wake is essentially periodic, the overall flow looses periodicity due to the far-wake convective disturbance growth.

IV.   DMD-BASED ANALYSIS OF THE TRANSVERSE SECONDARY INSTABILITY OF THE VON KARMAN VORTEX STREET

In the previous section, we investigated the structure of the two-dimensional flow past a permeable cylinder. However, actual flow configurations are intrinsically three-dimensional. In particular, the presence of modulations of the vortex shedding along the z (denoted as *spanwise*) direction is a crucial issue to characterize the behavior of cylindrical structures. In this perspective, we aim at understanding the conditions which lead to a destabilization of the two-dimensional von Karman vortex street along the spanwise direction through a *secondary* stability analysis of this periodic flow. The analysis of the emergence of three-dimensional instabilities of the two-dimensional von Kármán vortex street (*secondary instability*) typically relies on the Floquet analysis (see [33], [72]), whose formalism assumes a perfectly periodic vortex shedding in the whole domain, which is not the case in the present configuration. As a consequence, classical Floquet theory for the study of the secondary instability cannot be rigorously applied, unless one artificially filters out this far wake dynamics. This aspect does not affect the analysis
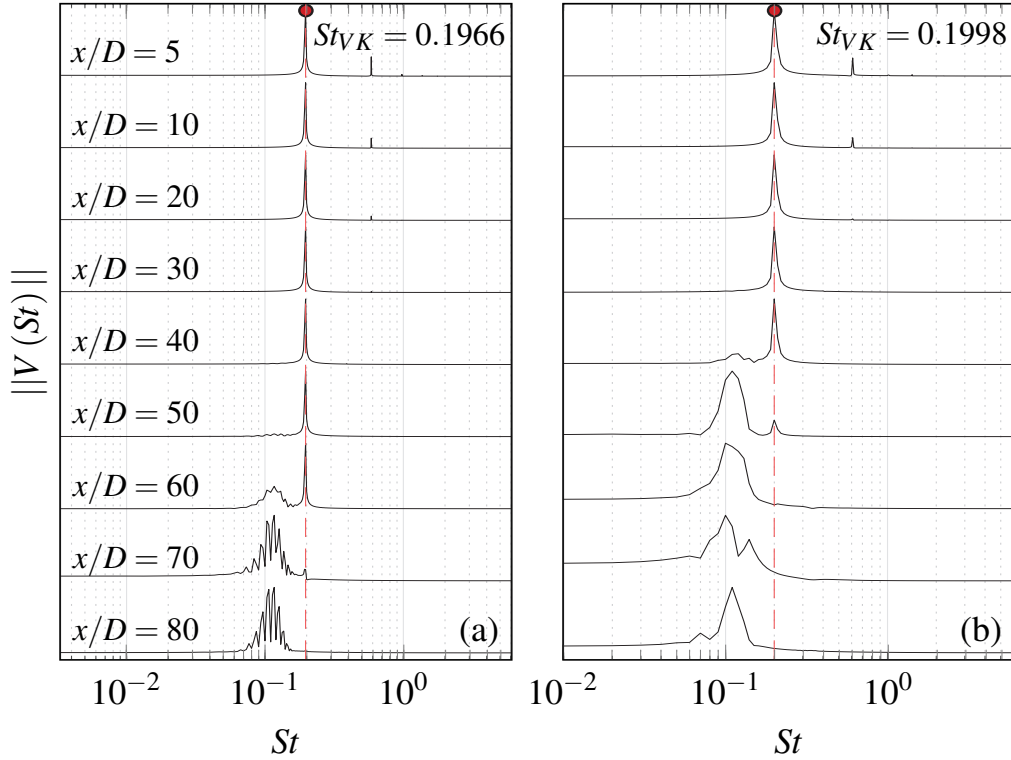
FIG. 9. Flow past a permeable circular cylinder: frequency spectra of the cross-stream component of velocity at different sample points in the streamwise locations and $y = 0$ for (a) $Da = 1 \times 10^{-4}$, $Re = 188.5$ and (b) $Da = 9 \times 10^{-4}$, $Re = 240$.

of the impervious case, but it may be important for the permeable case as the vortex street can originate significantly further downstream of the cylinder. A way to overcome this issue consists in applying an Arnoldi-like algorithm procedure only on a sub-domain of the field solution, specifically where the base-flow preserves the T-periodicity. As an alternative stability tool to study the emergence of these three-dimensional secondary modes, which reduces to the classical Floquet analysis when the flow is perfectly periodic but can handle cases with imperfect periodicity of the base flow, we propose here a procedure based on Dynamic Mode Decomposition (DMD), which also allows one to easily analyze smaller portions of the actual domain, so as to separate diverse dynamical behaviors occurring at different spatial locations, e.g. in the near and far wake.

It is well assessed in the literature [33] that the two-dimensional von Karman vortex street past a solid circular cylinder becomes unstable to transverse perturbations at $Re = 188.5$, leading to modulations of the vortex street past the cylinder. While the solid case has been widely investigated, similar studies in the permeable case are still lacking. In this section, we investigate the modifications induced by permeability on this transverse, secondary, instability. Following Barkley *et al.* [33], the three-dimensional instability is first induced by a long-wavelength mode A, which becomes unstable at $Re = 188.5$. A second family of modes (B), is characterized by shorter wavelengths and become unstable for $Re > 250$. Since we study the case $Re < 250$, we focus on the family of modes A, responsible for the first three-dimensional instability, in the impervious limit.

A. Linearized 3D equations

By introducing a $\mathscr{O}(\varepsilon)$ three-dimensional perturbation $(\mathbf{u}'(x,y,z,t), \quad p'(x,y,z,t), \quad p_i'(x,y,z,t))$, equations (1)-(3) are linearized around the time-dependent two-dimensional flow described in Section III B, i.e.

$$\mathbf{u}(x,y,z,t) = \mathbf{U}(x,y,t) + \varepsilon\mathbf{u}'(x,y,z,t), \quad p(x,y,z,t) = P(x,y,t) + \varepsilon p'(x,y,z,t), \quad p_i(x,y,z,t) = P_i(x,y,t) + \varepsilon p_i'(x,y,z,t), \quad (12)$$

Substitution into (1)-(3) leads to the following $\mathscr{O}(\varepsilon)$ linearized equations

$$\nabla \cdot \mathbf{u}' = 0, \quad \frac{\partial \mathbf{u}'}{\partial t} + u' \cdot \nabla \mathbf{U} + \mathbf{U} \cdot \nabla \mathbf{u}' - \nabla p' - \frac{1}{Re}\nabla^2 \mathbf{u}' = \mathbf{0}, \quad \nabla^2 p_i' = 0, \quad (13)$$

with homogeneous Dirichlet condition at the inlet and free-stress condition at the outlet and on the lateral boundaries. At the
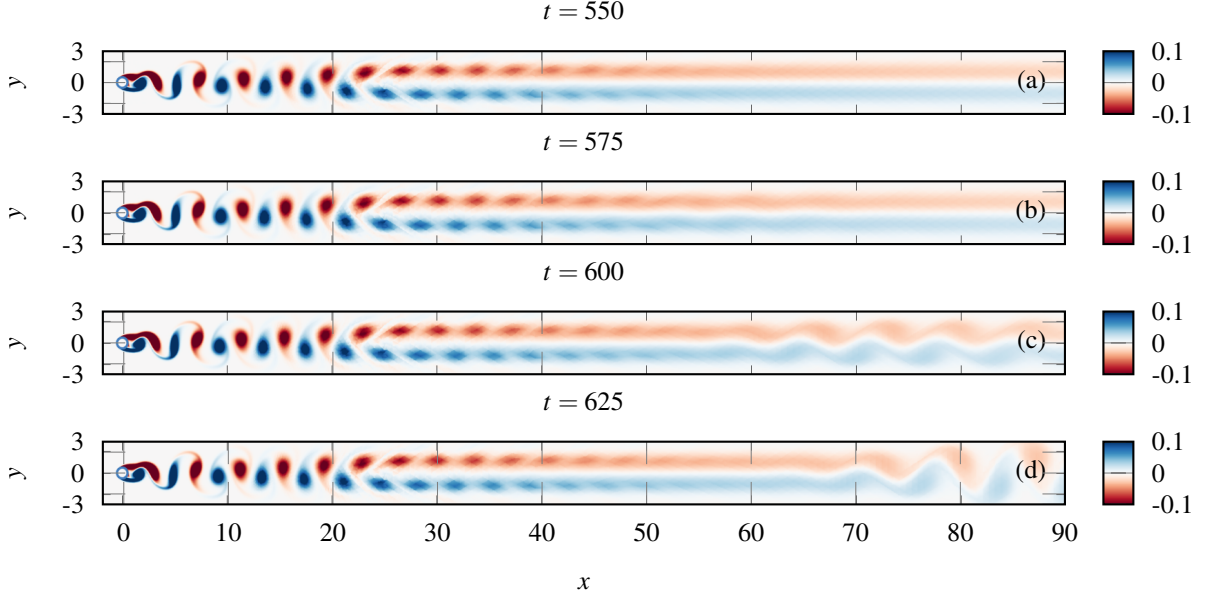
FIG. 10. Snapshots of the vorticity field iso-contours for $Da = 9 \times 10^{-4}$ and $Re = 240$.

interface Γ_{int}, the conditions below govern the dynamics of the three dimensional perturbation

$$\mathbf{u}'|_{\Gamma_{\text{int}}} = -ReDa\nabla p_i'|_{\Gamma_{\text{int}}} + \sqrt{Da}Re\left(\Sigma\left(\mathbf{u}',p'\right)|_{\Gamma_{\text{int}}}\mathbf{n}\right), \quad p_i'|_{\Gamma_{\text{int}}} = -\left(\Sigma\left(\mathbf{u}',p'\right)|_{\Gamma_{\text{int}}}\mathbf{n}\right)\cdot\mathbf{n}, \tag{14}$$

The small perturbation is given by the following real-valued ansatz:

$$\mathbf{u}' = \left(\tilde{u}(x,y,t)\cos(\beta z), \tilde{v}(x,y,t)\cos(\beta z), \tilde{w}(x,y,t)\sin(\beta z)\right), \tag{15a}$$

$$p' = \tilde{p}(x,y,t)\cos(\beta z), \quad p_i' = \tilde{p}_i(x,y,t)\cos(\beta z). \tag{15b}$$

Hence, for any combination (Re, Da), the three-dimensional linearized dynamics reduces to a one-parameter (the spanwise wavenumber β) family of two-dimensional problems.

Upon spatial discretization (see Section II for details), the linear system is conveniently rewritten as a dynamical system of ODEs:

$$\frac{d\tilde{\mathbf{q}}}{dt} = \mathscr{A}(t)\tilde{\mathbf{q}}, \tag{16}$$

where $\tilde{\mathbf{q}} = \{\tilde{\mathbf{u}}, \tilde{p}, \tilde{p}_i\}^T$, subjected to the initial condition $\tilde{\mathbf{q}}(t=0) = \tilde{\mathbf{q}}^{ic}$ which satisfies the boundary conditions. The temporal dependence of the unsteady two-dimensional base-flow is embedded in the linear operator $\mathscr{A}$. Note that if such operator is T-periodic, i.e. $\mathscr{A}(t) = \mathscr{A}(t+T)$, Floquet theory ensures an ansatz as [33]

$$\tilde{\mathbf{q}}(x,y,t) = \hat{\mathbf{q}}_F(x,y,t)\exp(\sigma_F t), \tag{17}$$

with $\hat{\mathbf{q}}_F(x,y,t) = \sum_{k=-\infty}^{k=+\infty}\phi_{F,k}(x,y)e^{ik\omega t}$ the Floquet mode associated with the potentially complex Floquet multiplier $\mu_F = \exp(\sigma_F T) = \exp(\sigma_F(2\pi/\omega))$, and where the real part of the Floquet exponent, $\text{Re}(\sigma_F)$, is related to the growth/decay rate of the perturbation. We also recall that a value of $\text{Im}(\sigma_F) = 0$ would mean that the unstable perturbation is synchronous with respect to the T-periodic base-flow [33].

B. SP-DMD algorithm for secondary stability analysis

The stability properties of the linear problem (16) are investigated through a Sparsity-Promoting Dynamic Mode Decomposition (SP-DMD) algorithm [42–44], whose essential points are introduced below. Dynamic Mode Decomposition relies on the formulation of the data-sequence as a *Krylov* sequence of snapshots $\hat{\mathbf{q}}_m$

$$\mathbf{Q}^m = \{\hat{\mathbf{q}}_0, \hat{\mathbf{q}}_2, ..., \hat{\mathbf{q}}_m\} \in \mathbb{R}^{n\times m}, \tag{18}$$
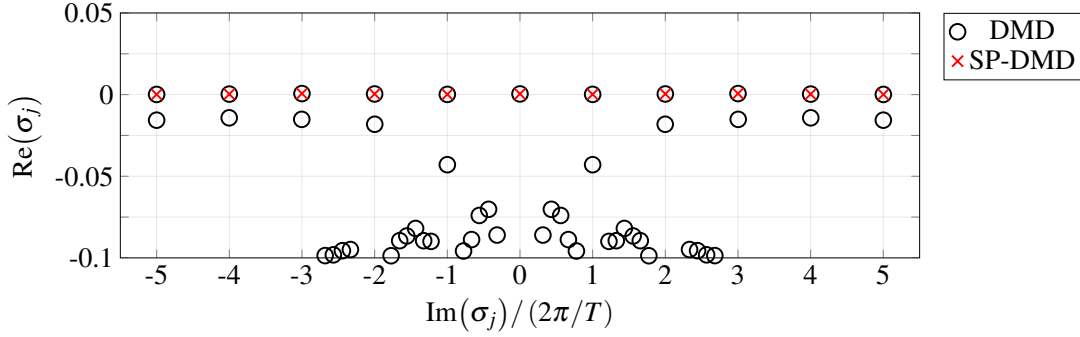
FIG. 11. Spectrum obtained from classic DMD (black circles) and Sparsity Promoting (SP) DMD (red crosses) for $(\beta, Da, Re) = (1.5, 9 \times 10^{-4}, 200)$. DMD-frequencies, $\text{Im}(\omega_j)$ are scaled with the oscillation frequency of the near wake base flow, $\omega = 2\pi/T$.

385 where n denotes the number of degrees of freedom and m is the number of equally spaced time-snapshots (separated by a
386 constant time-step Δt). The data-sequence is assumed here to be real-valued, i.e. $\in \mathrm{R}^{n \times m}$. Here snapshots $\hat{\mathbf{q}}_m$ are obtained
387 by time-integrating (16) for a fixed set of parameters, i.e. (Re, Da, β), starting from an initial condition $\{\hat{\mathbf{u}}^{ic}, \hat{p}^{ic}, \hat{p}_i^{ic}\}$. The
388 maximum time-step for time integration is 0.01. The time evolution of the perturbation field $\{\hat{\mathbf{u}}, \hat{p}, \hat{p}_i\}$ is then temporally
389 sampled with constant frequency with the constraint that $f > 2/T$ according to the Nyquist theorem, so as to obtain equally
390 spaced temporal snapshot separated by a time-step $\Delta t = 1/f$. In our specific case the value $f = 10$ is employed, corresponding
391 to about 50 snapshots per shedding cycle. Moreover, as we are mainly interested in characterizing the stability properties of the
392 near wake two-dimensional time-periodic flow dynamics, we can take advantage of the DMD technique to limit the analysis
393 only to a sub-portion of the actual domain, specifically, where the base flow is T-periodic. The sensitivity analysis to the size
394 of such a sub-domain reported in Appendix A shows that a spatial frame of extension $x \in (-1, 15)$ and $y \in (-4, 4)$ is a suitable
395 choice for the computation of the relevant DMD eigenvalues. For the sake of convenience, within this spatial window, the
396 flow fields corresponding to each temporal snapshot were interpolated from the original finite element grid onto a uniform grid
397 with $\Delta x = \Delta y = 0.8$. For specific cases, we employed a domain of streamwise extent up to $x = 60$, so as to better visualize the
398 downstream structure of the perturbation. Note that this does not affect the convergence of the results, as shown in Appendix A.
399   Without lack of generality, we chose as initial condition for the linearized simulations the time derivative of the base flow
400 $\partial \mathbf{U}/\partial t$, which naturally satisfies the boundary conditions and which essentially corresponds to a marginally stable Floquet mode
401 for a spanwise wavenumber $\beta = 0$ [33]. This choice helps in reducing the initial transient, which is then discarded.
402
403 We first introduce the two sub-snapshot matrices, $\mathbf{Q}_1^m = (\hat{\mathbf{q}}_0, \hat{\mathbf{q}}_1, ..., \hat{\mathbf{q}}_{m-1})$ and $\mathbf{Q}_2^m = (\hat{\mathbf{q}}_1, \hat{\mathbf{q}}_2, ..., \hat{\mathbf{q}}_m) \in \mathrm{R}^{n \times m-1}$. A pre-processing
404 step is performed, which employs the *economic-size* SVD decomposition of the data sequence $\mathbf{Q}_1^m$, i.e. $\mathbf{Q}_1^m = U\Sigma W^H$ (the
405 superscript "H" notes the conjugate transpose). The *companion* matrix $\tilde{S} = U^H \mathbf{Q}_2^m W \Sigma^{-1}$ is then computed, whose eigenvalues
406 and eigenvectors are solution of the following standard eigenvalue problem

$$\tilde{S} y_j = \mu_j y_j, \quad \phi_j(x, y) = U y_j, \quad \sigma_j = \log \mu_j / \Delta t, \tag{19a}$$

407 and represent the DMD eigenvalues and modes respectively. Quantities $\text{Re}(\sigma_j)$ and $\text{Im}(\sigma_j)$ have the meaning of a growth/decay
408 rate and oscillation frequency, respectively, associated with the jth DMD mode. As an example, the DMD spectrum computed
409 for the parameter setting $(Re, Da, \beta) = (200, 9 \times 10^{-4}, 1.5)$ is reported as black circles in figure 11. The data-sequence can be
410 then represented as

$$\mathbf{Q}_1^m \approx \sum_{j=1}^{r=m} \alpha_j \phi_j \mu_j^\tau = \phi D_\alpha V_{and}, \tag{20}$$

411 with $\tau \in (0, 1, ..., m-1)$, $\phi = (\phi_1, \phi_2, ..., \phi_r)$ (spatial structures), $D_\alpha = diag(\alpha)$ (amplitudes) and $V_{and} \in \mathrm{C}^{r \times m}$ the *Vandermonde*
412 matrix (temporal dynamics) [44].
413   At this stage, the vector of amplitudes, $\alpha = (\alpha_1, \alpha_2, ..., \alpha_r)$, is still unknown. In general, their determination requires solving
414 the following optimization problem,

$$\min_\alpha J(\alpha) := ||\mathbf{Q}_1^m - \phi D_\alpha V_{and}||_F^2 = ||\Sigma W^H - Y D_\alpha V_{and}||_F^2, \tag{21}$$

415 where the subscript "F" denotes the *Frobenius* norm and $J(\alpha)$ is the objective function.
416   In the present framework where DMD is used as a stability analysis tool to determine the eigenvalues and eigenmodes of the

system, we are not interested in reconstructing the original time process produced via linearized simulations, thus the determination of these amplitudes is not strictly relevant. However, it is known that the DMD algorithm presented above, requiring a matrix or pseudo-matrix inversion, often experiences numerical difficulties, due to the presence of several spurious modes [48]. In many cases, such modes can be successfully removed through an optimization process, i.e. Sparsity-Promoting (SP) algorithm [44], which identifies the modes that have the most profound influence on the quality of the approximation of the original snapshot-sequence. In practice, this is done by introducing a user-defined trade-off between the number of extracted modes and the approximation error with respect to the original data sequence, i.e. sparsity is induced by augmenting the objective function with an additional term that penalizes the l_1-norm of the vector of unknown amplitudes α. Hence, the amplitude calculation is still useful in this context so to filter out spurious modes and to highlight the dominant modes in the eigenvalue spectrum of figure 11. The problem of computing these amplitudes takes the form of a constrained convex optimization problem (solvable via *Alternating direction method of multipliers* (ADMM) [44]). Further details are given in [44]. The Matlab function implementing the Sparsity Promoting algorithm, used in the present work, can be found in [73].

The optimized SP-DMD eigenvalues are reported in figure 11 as red crosses. We recall that the DMD analysis is performed in a sub-domain where the unsteady two-dimensional base flow is T-periodic so to filter our the secondary dynamics in the far wake base flow. Then, for the parameter configuration of figure 11, the SP algorithm identifies as dominant a series of aligned modes sharing the same growth rate Re(σ_j)= σ_{DMD}, e.g. zero in this case (marginally stable at $\beta = 1.5$), and corresponding to consecutive harmonics, i.e. Im(σ_j)= $l\omega$, $l = \ldots, -2, -1, 0, 1, 2, \ldots$, with the first harmonic for $l = \pm 1$, synchronized with the oscillation frequency of the T-periodic base flow.

Thus, given the properties of the SP-DMD spectrum of figure 11, from equation (20) one can readily construct a basis of DMD modes in the following form

$$\exp(\sigma_{\mathrm{DMD}}(\tau\Delta t)) \sum_{l=-N_h}^{l=+N_h} \phi_l(x,y) e^{il\omega(\tau\Delta t)}, \tag{22}$$

where N_h denotes the number of harmonics considered in the computation whereas the index l is here used to refer to the SP-DMD mode corresponding to each of those harmonics. Note that the amplitudes have been omitted for the sake of clarity. As already outlined in [48], the close connection with Floquet modes appears straightforward once recalling the standard Floquet ansatz

$$\exp(\sigma_F t) \sum_{k=-\infty}^{k=+\infty} \phi_{F,k}(x,y) e^{ik\omega t}, \tag{23}$$

with Im(σ_F)= 0 for a synchronous instability. Essentially, the set of DMD modes identified by the SP algorithm gives an approximation of the dominant Floquet mode. Note that it is only an approximation because of the truncated series in (22). Furthermore, for $\tau\Delta t = T$, $exp(\sigma_{DMD}(\tau\Delta t)) = exp(\sigma_{DMD}T)$ precisely corresponds to the Floquet multiplier $\mu_F = exp(\sigma_F T)$, which we will denote hereinafter simply as $\mu \in$ R and that will be used as criterion for the determination of the instability onset, e.g. $\mu < 1$ stable, $\mu = 1$ marginally stable and $\mu > 1$ unstable, keeping in mind that this calculation is not performed via standard Floquet analysis, but rather through a SP-DMD algorithm that post-processes linearized simulations.

In summary, the DMD computation provides several harmonics, all associated with the same multiplier, which composed together provide the Floquet eigenmode.

In Appendix A we validate the outcomes of our DMD-base procedure with those of Barkley & Henderson [33], for the case of a solid cylinder, from a standard Floquet analysis. To this end we replicated their exact domain size and we employed a comparable mesh. In Table III is reported the variation of the multiplier μ with respect to the spatial window employed for the assembling of the snapshot matrix Q^m. The grid coincides with the one employed for the two-dimensional time-dependent nonlinear simulations.

C. Results

Figure 12 shows the spatial distributions of the late-time z-vorticity, obtained from the linearized model, for $Da = 9 \times 10^{-4}$ and for increasing Reynolds numbers, while figure 13 shows the associated time-evolution of the y-component of velocity of the three-dimensional perturbation sampled at $x = 2.5$. In case (a), we report a snapshot for a case in which the three-dimensional perturbation is decaying with time. We observe the presence of two regions. In the vicinity of the body, the vorticity distribution is similar to that of mode A for impervious cylinders [33]. Conversely, far downstream, vorticity cores stretch along the streamwise direction and get closer to the axis $y = 0$. In panels (b,c), we instead report two unstable cases. The pattern of streamwise vorticity in the near-wake is similar to that of mode A past impervious cylinders [33]. In case (b), the amplitude of vorticity is spatially decaying while moving downstream, in opposition to case (c), where the amplitude of vortical structures increases with x.
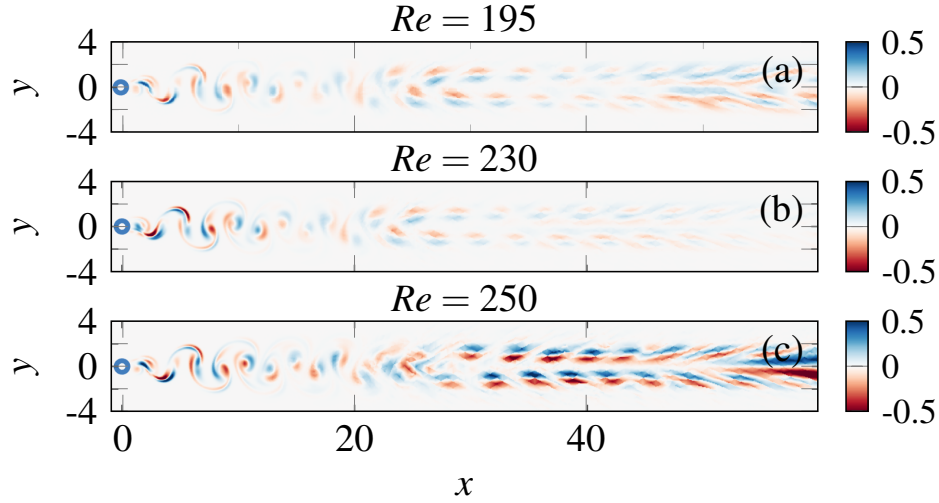
FIG. 12. Spanwise (z) component of vorticity (rescaled with its maximum absolute value) from the linearized simulations at $t = 100$ and $Da = 9 \times 10^{-4}$": (a) $Re = 195$, $\beta = 1.56$, (b) $Re = 230$, $\beta = 1.5$ and (c) $Re = 250$, $\beta = 1.5$.
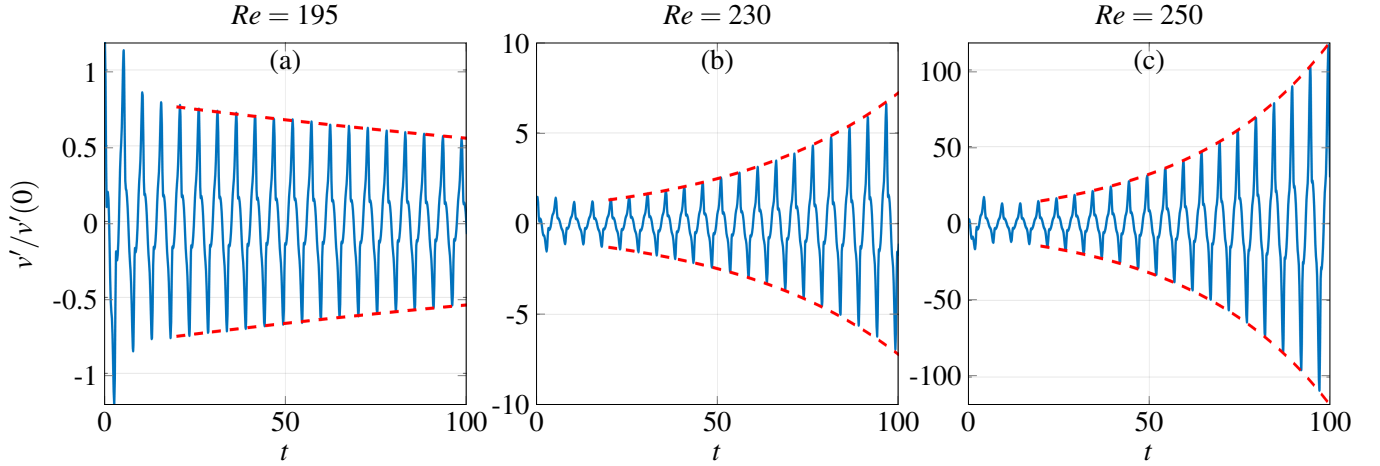

FIG. 13. $Da = 9 \times 10^{-4}$. Transversal velocity $\tilde{v}$ sampled at $(x = 2.5, y = 0)$ as a function of time. The red dashed line denotes the exponential growth or decay obtained from DMD. (a) $Re = 195$ and $\beta = 1.56$, (b) $Re = 230$ and $\beta = 1.5$, (c) $Re = 250$ and $\beta = 1.5$.

The downstream displacement in the onset of the three-dimensional perturbation is related to the downstream shift in the formation of the two-dimensional vortex shedding, induced by the permeability of the cylinder. The evolution of the 3D perturbation is reminiscent of the three regions observed in figure 8. Initially, the perturbation vorticity follows the vortex shedding pattern. For $10 < x < 20$, the transitional behavior is observed both for the base flow and perturbation. At large distances, the baseflow presents two shear layers of opposite vorticity. The perturbation is instead characterized by patches of opposite vorticity on each half-plane that progressively stretch.

As seen in figure 13, case (a) is characterized by a decreasing amplitude of the oscillations with time, while cases (b,c) are unstable and the perturbation grows. The temporal evolution is a T-periodic function modulated by a decaying or growing exponential. Upon employment of the DMD-based procedure on the linearized simulations, one obtains the Floquet multiplier μ and the associated eigenvectors, for each value of β, Re and Da considered. The Floquet multiplier allows for the temporal reconstruction of the envelope of the perturbation, reported with the dashed line in figure 13, which shows that the exponential growth predicted using the DMD technique is in excellent agreement with the envelope of the decaying or growing perturbation.

The Floquet multipliers and modes depend on the spanwise wavenumber β. For varying β, one obtains the dispersion relation, which relates the behavior in space (z) and time of the growing or damped perturbation. Figure 14 presents diverse dispersion relations for different values of permeability and Reynolds number. All dispersion relations have a similar behavior, characterized by a maximum of μ in an intermediate range of β. We begin by considering subfigure (a), i.e. $Da = 10^{-4}$. For this value of permeability, the dispersion relation is analogous to the one of an impervious cylinder. For $Re = 180$, the maximum value of μ
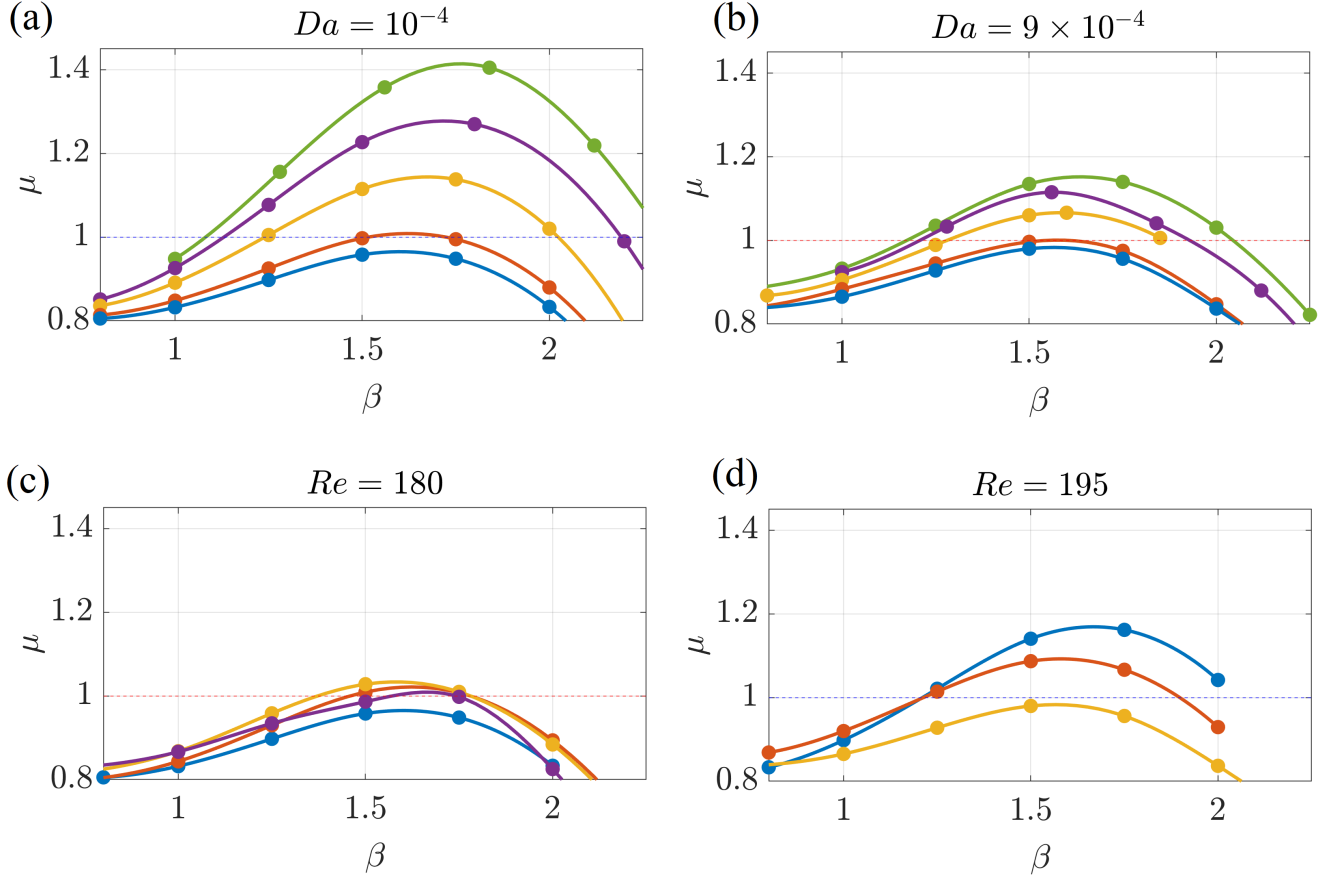
FIG. 14. Dispersion relations for different cases. (a) $Da = 10^{-4}$ and increasing Reynolds number; $Re = 180$ (blue), $Re = 185$ (orange), $Re = 200$ (yellow), $Re = 215$ (purple), $Re = 230$ (green). (b) $Da = 9 \times 10^{-4}$ and increasing Reynolds number; $Re = 195$ (blue), $Re = 200$ (orange), $Re = 215$ (yellow), $Re = 230$ (purple), $Re = 250$ (green). (c) $Re = 180$ and increasing Darcy number; $Da = 10^{-4}$ (blue), $Da = 2.5 \times 10^{-4}$ (orange), $Da = 5 \times 10^{-4}$ (yellow), $Da = 7 \times 10^{-4}$ (purple). (d) $Re = 195$ and increasing Darcy number; $Da = 2.5 \times 10^{-4}$ (blue), $Da = 7 \times 10^{-4}$ (orange), $Da = 9 \times 10^{-4}$ (yellow).Note that the solid lines are obtained via *spline*-interpolation and only serve to guide the eye.

is less than unity. A slight increase in the Reynolds number ($Re = 185$) increases the value of the Floquet multiplier, and there is a small range of β for which $\mu > 1$. We identify the presence of two *cut-off* wavenumbers which identify the crossing $\mu = 1$. A further increase in Re leads to a progressive enlargement of the region with $\mu > 1$, and at the same time the maximum value of the Floquet multiplier increases. An increase in permeability (subfigure (b)) leads to similar trends, although the maximum value of μ decreases. Subfigure (c) instead shows the dispersion relations for fixed Reynolds number $Re = 180$ and increasing values of permeability. As Da increases, the maximum value of μ increases. For $Da = 2.5 \times 10^{-4}$, a range with $\mu > 1$ appears, which enlarges for $Da = 5 \times 10^{-4}$ and eventually shrinks for $Da = 7 \times 10^{-4}$, as the maximum value of μ decreases. For $Re = 195$ (subfigure (d)), a stabilizing effect with increasing Da is observed.

In summary, an increase in Reynolds number leads to an overall increase of μ. Conversely, an increase in Da instead leads to a non-monotonous behavior of μ, characterized by an initial increase for low permeabilities followed by a decrease at large permeabilities, as shown in figure 14(c). The dispersion relations show the typical behavior described by Barkley [33] for the impervious case, with a maximum μ and two cut-off wavenumbers for which $\mu = 1$. Therefore, the two cut-offs define the unstable range of wavenumbers. Figure 15 summarizes the behavior of the maximum value of μ (obtained through the spline interpolation shown in figure 14) and the associated β in the (Da, Re) plane, for the studied cases in the range $175 < Re < 250$, together with a linear interpolation to $\mu = 1$ (red line) that indicates the location of the marginal stability conditions. As already observed, the unstable range of wavenumbers where $\mu > 1$ initially slightly increases with the permeability. This is correlated to the slight decrease of the critical Reynolds number observed in the (Da, Re) plane. However, for $Da > 5 \times 10^{-4}$, the critical Reynolds number presents a very steep increase. This steep increase allows us to define a critical value of permeability $Da \approx 10^{-3}$, valid at least in the considered range of Reynolds numbers. Beyond this value, no growing perturbations have been observed in our linearized simulations performed for $Da = 2 \times 10^{-3}, 3 \times 10^{-3}$ and $Re = 200, 215, 230$. The value of the estimated wavenumber associated with the maximum Floquet multiplier shows only a variation of $\approx 6\%$ near the marginal
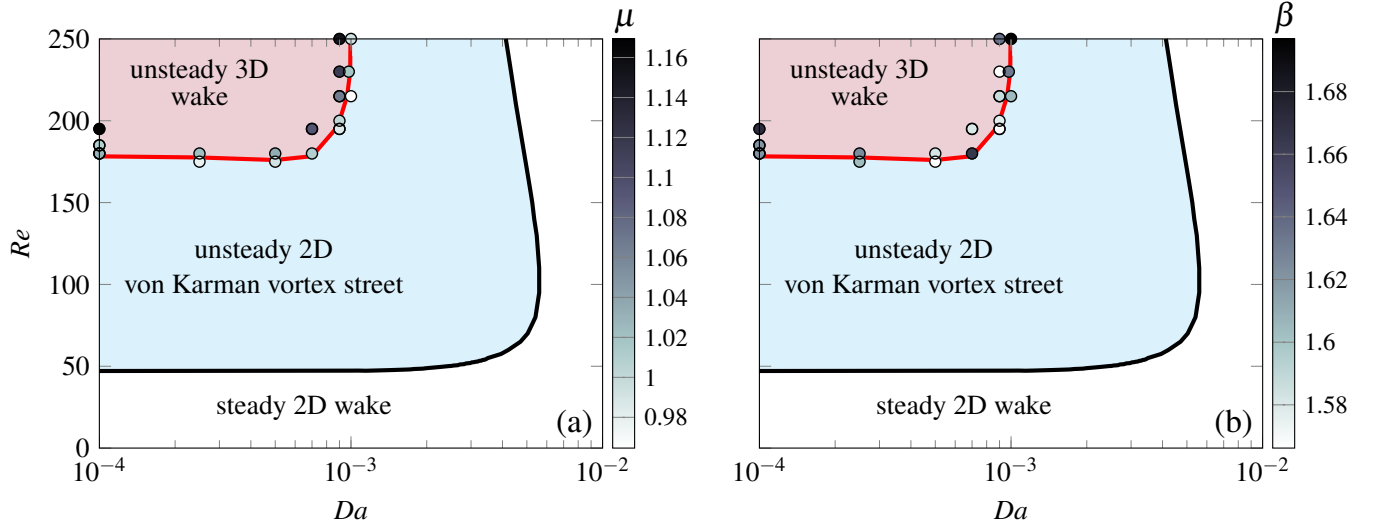
FIG. 15. Scatter plot of (a) the maximum value of μ and (b) its associated wavenumber β, in the (Da, Re) plane. The red line sketches the marginal stability curve for three-dimensional instability inferred from the values of μ. The black line instead denotes the marginal stability curve for the onset of the two-dimensional von Karman vortex street. These lines define three regions with different patterns in the $Da - Re$ plane: steady and two-dimensional wake (white), unsteady 2D von Karman vortex street (cyan), unsteady 3D wake (light red).
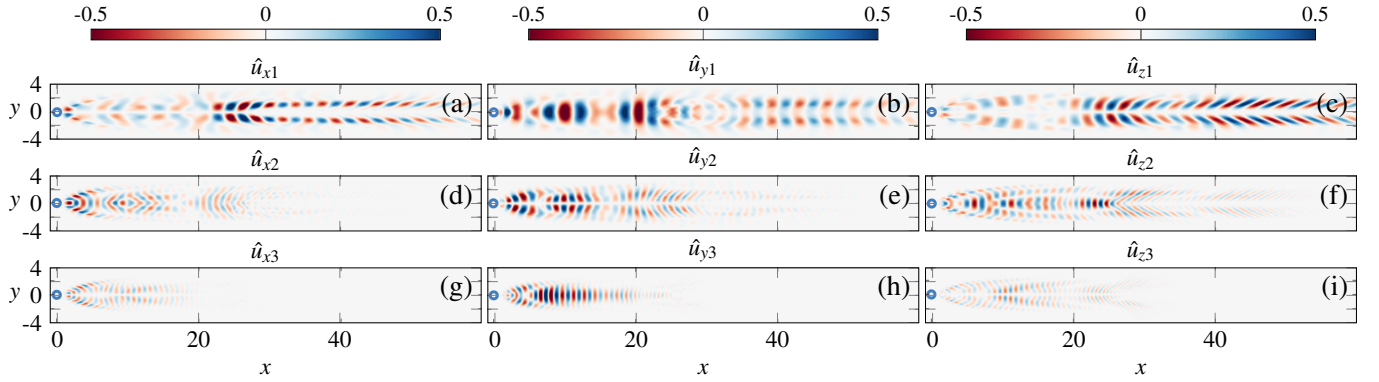

FIG. 16. Modal form of (a,d,g) first, (b,e,h) second and (c,f,i) third harmonic of the linearized velocity field, for $Re = 195$, $Da = 9 \times 10^{-4}$, and $\beta = 1.5$. Each harmonic is scaled with the corresponding maximum absolute value.

502 stability conditions.

503   Figure 15 defines three regions in the (Da, Re) space. The first one is bounded by the black curve and corresponds to the
504 region where the steady two-dimensional wake is linearly stable, and it has been confirmed using time-dependent, non-linear,
505 simulations. The black and red lines instead define a region in which the two-dimensional periodic vortex shedding past a
506 permeable cylinder is linearly stable with respect to the 3D A-mode. Interestingly, there is a range of permeability for which
507 the steady two-dimensional wake appears to be linearly stable, for $Re < 250$ at least, as investigated in this study. Finally, the
508 region enclosed by the red curve identifies the parameter combinations in which spanwise modes are amplified and lead to three-
509 dimensional dynamics. The marginal curve which separates the two-dimensional and three-dimensional dynamics obtained
510 through linear stability analysis resembles the one which separates steady and unsteady two-dimensional wake. It delineates a
511 minimal permeability which suppresses three-dimensional instabilities. The presence of a region in which the two-dimensional
512 von Karman vortex street appears to be stable is associated with negligible lift forces on the body (see figure 7). Therefore,
513 highly permeable three-dimensional cylinders are characterized by a stable two-dimensional vortex shedding, but there are no
514 significant oscillating forces acting on the body.

515   To complete our characterization of the three-dimensional instability, we now turn to describe the spatial structure of the modes
516 near the marginal stability curve. Figure 16 shows the first three harmonics of the velocity field, for $Re = 195$ and $Da = 9 \times 10^{-4}$.
517 The first harmonic of the x and y components of velocity strongly resembles the vortex shedding mode obtained through linear
518 stability analysis (see figure 8), in the vicinity of the body. However, the modes significantly change when moving downstream.
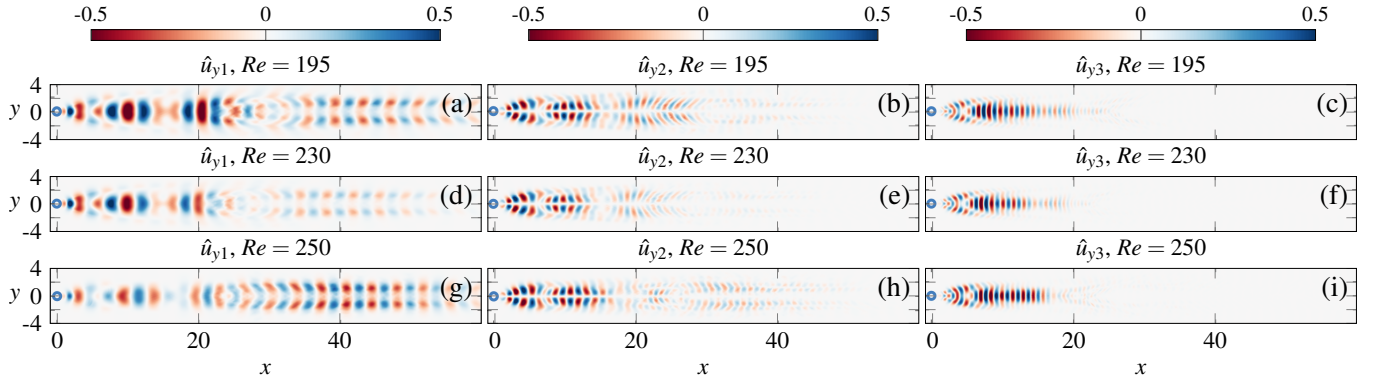
FIG. 17. Modal form of (a,d,g) first, (b,e,h) second and (c,f,i) third harmonic, for $Da = 9 \times 10^{-4}$ and $Re = 195$ (top), $Re = 230$ (center) and $Re = 250$ (bottom), rescaled with the corresponding maximum absolute value.

The streamwise component of the velocity field re-organizes in the region $10 < x < 20$. For $x > 20$, structures of alternating signs dominate the dynamics, antisymmetric with respect to $y = 0$ and of larger amplitude and with shorter streamwise extent than the structures observed upstream. These structures progressively re-align along the downstream direction while they decrease their amplitude. A similar behavior is observed for the first harmonic of the y component of velocity. A mode reminiscent of the vortex shedding re-organizes in structures of alternating sign, symmetric with respect to the y axis. Their maximum amplitude is located in the vicinity of the cylinder, in opposition to the streamwise component. Also the spanwise component of velocity exhibits a re-organization for $10 < x < 20$, which leads to structures of large amplitude and alternating sign, antisymmetric with respect to the y axis, that are damped for $x > 50$. The velocity components of the second and third harmonics instead present structures of smaller streamwise extent, rapidly damped when moving downstream, in the transition region of the first harmonic. Moreover, the third harmonic decays at a distance from the cylinder smaller than the second harmonic case. The effect of the Reynolds number on the spatial structure of the modes, in the vicinity of the marginal stability conditions, is reported in figure 17, for the y component of the velocity field. An increase in Re does not modify qualitatively the observed behavior, with an upstream region reminiscent of the vortex shedding mode and a downstream one characterized by alternating structures symmetric with respect to the y axis, of smaller streamwise extent. However, the amplitude of the first harmonic in the upstream region reduces (with respect to the maximum absolute value of velocity) and, at $Re = 250$, becomes larger in the downstream region. The second and third harmonic remain similar when the Reynolds number increases.

The analysis of the spatial structure of the modes identified by DMD shows that the first harmonic is persistent for approximately $x < 60$, while the harmonics are rapidly damped when moving downstream. Therefore, the downstream linearized dynamics is dominated by a mode whose frequency coincides with the one of the vortex shedding. The effect of harmonics is appreciable in the region where the vortices form and detach. The harmonics present alternating structures of smaller streamwise extent since an increase in the shedding frequency, with the same advection, leads to smaller structures shed from the cylinder. In the vicinity of the marginal stability threshold, Re does not strongly affect the observed patterns. It is also interesting to note that the instability is present also in the vicinity of the cylinder, while the marginally stable two-dimensional modes of the steady baseflow were localized more downstream. This is due to the fact that the suppression of the three-dimensional instability occurs at values of permeability significantly lower than the ones for the quenching of the von Karman vortex street, where the recirculation region of the mean flow is localized in the vicinity of the body. The primary effect of permeability on the three-dimensional instability is the modification of the threshold for the instability, while the unstable wake patterns are similar to the impervious case.

The physical mechanism underlying this stabilization of the 3D instability tentatively lies in the weakening of the deformation of the vortex cores, which can be qualitatively appreciated in figure 8. Comparing for instance panels (c) and (a), vortices forming in the wake of the more permeable cylinder are less stretched along the streamwise direction. This decreased stretching effect is caused by a lower strain rate in the vortex centers with increasing permeability. When the strain rate becomes too small (i.e. the more permeable case), the inviscid elliptic instability mechanism becomes too weak to overcome viscous damping [74] and the instability is quenched.

V. CONCLUSION

In this work, the two-dimensional flow in the wake past a permeable circular cylinder and its stability properties are studied. Two subsequent instabilities are investigated, i.e. the primary instability leading to a two-dimensional vortex shedding and the three-dimensional instability of the wake. The steady two-dimensional flow presents a recirculation region that detaches

from the cylinder and is shifted downstream as permeability is increased. The length of the recirculation region and the drag coefficient are correlated and they are non-monotonous with respect to permeability, the drag coefficient having a maximum at intermediate permeabilities before decreasing monotonically. Linear stability analysis of the steady two-dimensional flow is applied for the identification of the stable and unstable regions in the (Da, Re) parameter space. The primary instability, when present, leads to the formation of vortex shedding. Since vortex shedding is related to the recirculation region of the unstable steady configuration, it is observed that the formation of alternate vortices starts progressively more downstream as permeability increases. As a result, while in the impermeable case vortices form in the rear of the cylinder, the permeable case shows the formation of two vorticity layers which extend at a distance of some diameters past the cylinder, beyond which alternating vortices emerge. This downstream displacement implies a progressive damping of the oscillations of aerodynamic forces acting on the body. However, the mean value of drag coefficient shows a maximum at intermediate permeabilities, before decreasing monotonically. Finally, the shedding frequency increases moving away from the marginal stability conditions, both in terms of permeability and Reynolds number.

The strong modifications of the vortex shedding underlies different stability properties with respect to spanwise, three-dimensional perturbations. On this regard, a Sparsity-Promoting Dynamic Mode Decomposition (SP-DMD) is applied to snapshot sequences produced by the linear temporal evolution of three-dimensional disturbance. Hence, SP-DMD is used here as an alternative linear stability analysis tool, since it is capable of predicting the relevant structures and growth rates, in the form of DMD eigenmodes and eigenvalues, respectively, as well as the most unstable wavenumbers. The resulting dispersion relations, which are derived here as a function of Da, are similar to those of the impervious case, although the growth rate significantly depends on the permeability. Besides the quantitative differences in the growth rates, the critical Reynolds number for the three-dimensional instability is affected by permeability. In particular it slightly decreases at intermediate permeabilities while, for $Da \approx 10^{-3}$, it strongly increases, identifying this as an approximate critical value of permeability beyond which the vortex shedding remains two-dimensional in the explored range of flow parameters.

The present work aims at giving an insight into unsteady patterns of the wake past a permeable circular cylinder, with focus on its three-dimensional stability and how this depends on permeability. Moreover, it demonstrates that SP-DMD can be used as an effective tool to perform the stability analysis of complex flows involving three-dimensional instabilities as the one at issue here. As possible extensions of this research activity toward Reynolds numbers larger than the one considered here, we believe that an important improvement, both in the analysis and from a methodological viewpoint, would be the inclusion of inertia through the pores by considering a steady flow at the microscopic scale in the limit of $Re_p = \mathcal{O}(1)$ within the pores, through an Oseen approximation [54]. This extension would help in better describing the flow past bodies of large permeability and/or microscopic characteristic length (see [9] for thin permeable bodies), and extend the range of considered Reynolds number. This could pave the way toward the analysis of phenomena such as air-grass interactions (*honami-flows*), water-seagrass interactions (*monami-flows*) [75, 76], flows within catalytic reactors and through heat exchangers [77] or flows over built-up urban areas [78]. Moreover, larger Reynolds numbers could lead to unsteadiness and even three-dimensionality at the pore level and further studies may include these effects stemming from the structure arrangement at the pore level over the macroscopic problem.

CONFLICT OF INTEREST

The authors declare no conflict of interest.

Appendix A: Grid convergence analysis and verification of the numerical approach

In this section, we first report the mesh convergence analysis for the linear stability analysis, performed with respect to the critical Reynolds number and frequency for the primary instability. For primary instability, we intend the plane two-dimensional instability that leads the flow from steady to unsteady (periodic-in-time). While a first verification was made on the impervious value of critical Reynolds number for the onset of vortex shedding, for the grid convergence analysis, we consider a case with large permeability and Reynolds number. To verify the mesh convergence, we (i) vary the downstream, upstream and lateral position of the boundary, and (ii) increase the mesh resolution. In table I (upper part) results for different domains are reported, obtained by progressively increasing each side of the rectangular domain. The progressive variation of the computational domain is performed with constant resolution along the domain's edges. In the lower part of table I, we instead report the results with varying mesh resolution. The critical Reynolds number is well predicted with mesh M4, with a tolerance on the value of $Re < 1$
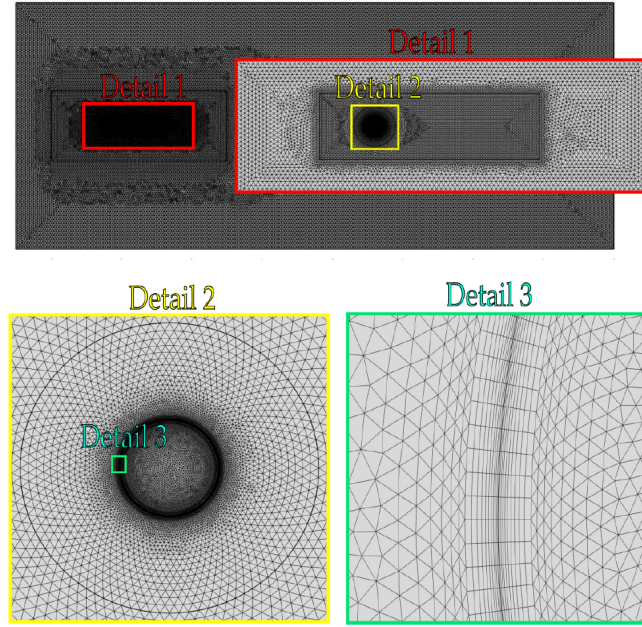
FIG. 18. Computational domain and refinements for mesh M4.

Mesh name	$x_{-\infty}$	$x_{+\infty}$	y_∞	N_{el}	Re_{cr}	$\mathrm{Im}(\sigma)$
M4-downstream A	30	160	35	116154	204	0.82
M4-downstream B	30	180	35	123528	204	0.82
M4-downstream C	30	220	35	137928	204	0.83
M4-upstream A	40	140	35	113064	205	0.82
M4-upstream B	50	140	35	116970	205	0.82
M4-lateral	30	140	45	127526	205	0.83
M1	30	140	35	41426	204	0.83
M2	30	140	35	52874	204	0.83
M3	30	140	35	78914	204	0.83
M4	30	140	35	108834	204	0.82
M5	30	140	35	186138	204	0.83
M6	30	140	35	284234	204	0.83

TABLE I. Mesh convergence for the case $Da = 4.6 \times 10^{-3}$. The upstream and downstream boundary locations are denoted as $x_{-\infty}$ and $x_{+\infty}$, respectively, while y_∞ denotes the position of the lateral boundaries. The total number of elements of the mesh is denoted as N_{el}.

and relative error less than 1%, between all considered mesh and the one with finest resolution. A similar result is obtained for the oscillation frequency. Therefore, we conclude that mesh M4 (reported in figure 18) is suitable for the linear stability analysis parametric study with, at most, a relative tolerance of 1% on the critical value of Reynolds and Strouhal numbers. This mesh has been employed for the stability analysis.

A similar analysis on the domain size with grids derived from mesh $M4$ is performed for the time-dependent non-linear simulations, as reported in table II. Variations of the Strouhal number are negligible, while the drag and lift coefficients vary less than 0.1%.

Figure 19 shows the domain employed for the DMD-based algorithm, which is applied in a subdomain of the domain employed

L_{out}	St	$\bar{C}_d$	C_L^{max}
90	0.199	1.435	0.256
120	0.199	1.434	0.256
140	0.199	1.434	0.256

TABLE II. Variation of Strouhal number, drag and lift coefficients with respect to the domain size, for $Da = 9 \times 10^{-4}$ and $Re = 195$. The non-linear time-dependent simulations are performed adopting a grid derived from mesh M4 where elements are progressively subtracted in the outflow region decreasing the outflow length up to $L_{\mathrm{out}} = 90$.
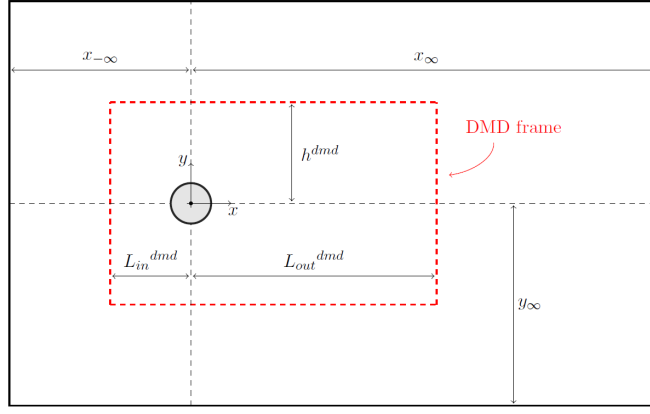
FIG. 19. Spatial subdomain used in the DMD analysis together with relevant dimensions.

L_{out}	L_{out}^{dmd}	T_{fin}	μ
140	30	120	0.97823
140	30	100	0.97824
140	30	80	0.97821
140	75	120	0.97823
140	50	120	0.97823
140	30	120	0.97823
140	15	120	0.97823
140	7.5	120	0.9782
140	15	120	0.97823
120	15	120	0.97803
90	15	120	0.97997

TABLE III. Convergence of the multiplier μ calculated through the DMD algorithm, Re=195, $Da = 9 \times 10^{-4}$ and $\beta = 1.5$. L_{out} denotes the outlet position employed in the linearized simulations, while L_{out}^{dmd} the outlet employed for the DMD frame; T_{fin} instead denotes the final time considered in the linearized simulations and for the DMD-based analysis.

614 for the linear, time-dependent, simulations. The variation of the Floquet multiplier between all cases, reported in table III, is less
615 than 0.1% and thus acceptable for the considered parametric study.
616   Lastly, in figure 20 we report a verification of our DMD-based procedure used in the computation of the Floquet multipliers μ
617 as outlined in Sec.IV B. More precisely, by setting the Darcy number to a value $Da = 1 \times 10^{-4}$, which approximately corresponds
618 to the case of a solid cylinder, we reproduce pointwise the results extracted by figure 5 of Barkley & Henderson [33]. We see
619 that the red filled markers, which have been produced by our DMD-based eigenvalue calculation, are in fairly good agreement
620 with those of Ref.33 for different Reynolds numbers Re and spanwise wavenumbers β.

621 [1] M. P. Paidoussis, *Fluid-structure interactions: slender structures and axial flow*, Vol. 1 (Academic press, 1998).
622 [2] C. H. Williamson, R. Govardhan, *et al.*, Vortex-induced vibrations, Annual review of fluid mechanics **36**, 413 (2004).
623 [3] O. Flamand, Rain-wind induced vibration of cables, Journal of Wind Engineering and Industrial Aerodynamics **57**, 353 (1995).
624 [4] E. Boujo, A. Fani, and F. Gallaire, Second-order sensitivity in the cylinder wake: Optimal spanwise-periodic wall actuation and wall
625   deformation, Physical Review Fluids **4**, 053901 (2019).
626 [5] B. Drew, A. R. Plummer, and M. N. Sahinkaya, A review of wave energy converter technology (2009).
627 [6] A. Nitti, G. De Cillis, and M. de Tullio, Cross-flow oscillations of a circular cylinder with mechanically coupled rotation, Journal of Fluid
628   Mechanics **943** (2022).
629 [7] Q. Y. Z. G. Lee, Y.J. and K. B. Lua, Vortex-induced vibration wind energy harvesting by piezoelectric mems device in formation, Scientific
630   Reports **9**, 20404 (2019).
631 [8] G. Falcucci, G. Amati, P. Fanelli, V. K. Krastev, G. Polverino, M. Porfiri, and S. Succi, Extreme flow simulations reveal skeletal adapta-
632   tions of deep-sea sponges, Nature **595**, 537 (2021).
633 [9] P. Ledda, E. Boujo, S. Camarri, F. Gallaire, and G. Zampogna, Homogenization-based design of microstructured membranes: wake flows
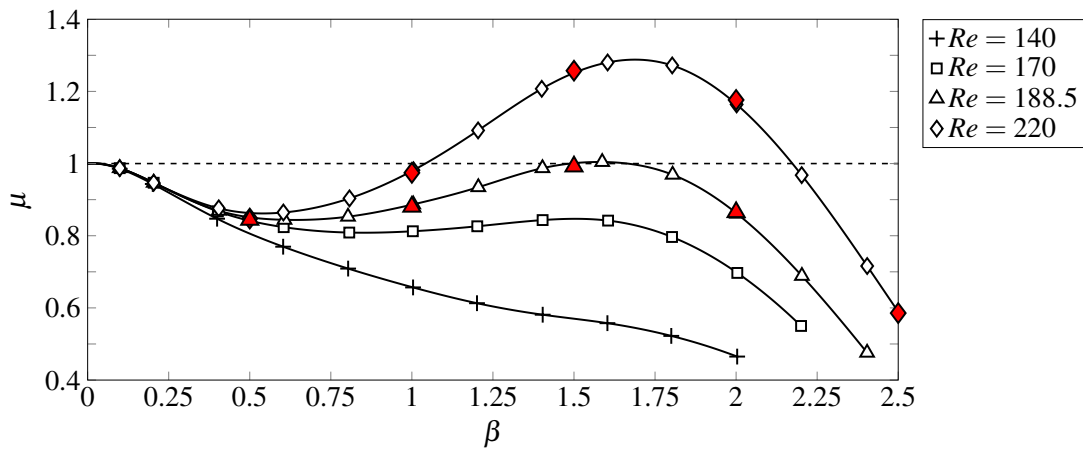634   past permeable shells, Journal of Fluid Mechanics **927**, A31 (2021).

FIG. 20. Dependence of the dominant Floquet multiplier μ on spanwise wavenumber β for four different values of Re. The white markers and black solid lines correspond to those reported in figure 5 of Barkley & Henderson [33] for the case of a solid cylinder. On the other hand, the red filled markers denote the Floquet multipliers computed via the DMD-based procedure outlined in Sec.IV B of this work and obtained by setting a Darcy number $Da = 1 \times 10^{-4}$, so as to approximate the solid case.

[10] E. Boujo and F. Gallaire, Controlled reattachment in separated flows: a variational approach to recirculation length reduction, Journal of Fluid Mechanics **742**, 618 (2014).

[11] C. Cummins, M. Seale, A. Macente, D. Certini, E. Mastropaolo, I. Viola, and N. Nakayama, A separated vortex ring underlies the flight of the dandelion, Nature **562**, 414 (2018).

[12] C. Cummins, I. M. Viola, E. Mastropaolo, and N. Nakayama, The effect of permeability on the flow past permeable disks at low Reynolds numbers, Physics of Fluids **29**, 097103 (2017).

[13] P. G. Ledda, L. Siconolfi, F. Viola, S. Camarri, and F. Gallaire, Flow dynamics of a dandelion pappus: A linear stability approach, Physical Review Fluids **4**, 071901 (2019).

[14] I. P. Castro, Wake characteristics of two-dimensional perforated plates normal to an air-stream, Journal of Fluid Mechanics **46**, 599 (1971).

[15] K. Steiros, K. Kokmanian, N. Bempedelis, and M. Hultmark, The effect of porosity on the drag of cylinders, J. Fluid Mech **901**, R2 (2020).

[16] K. Steiros and M. Hultmark, Drag on flat plates of arbitrary porosity, Journal of Fluid Mechanics **853**, R3 (2018).

[17] E. F. Strong, M. Pezzulla, F. Gallaire, P. Reis, and L. Siconolfi, Hydrodynamic loading of perforated disks in creeping flows, Physical Review Fluids **4**, 084101 (2019).

[18] M. Pezzulla, E. F. Strong, F. Gallaire, and P. M. Reis, Deformation of porous flexible strip in low and moderate Reynolds number flows, Physical Review Fluids **5**, 084103 (2020).

[19] L. Zong and H. Nepf, Vortex development behind a finite porous obstruction in a channel, Journal of Fluid Mechanics **691**, 368 (2012).

[20] A. Nicolle and I. Eames, Numerical study of flow through and around a circular array of cylinders, Journal of Fluid Mechanics **679**, 1 (2011).

[21] P. G. Ledda, L. Siconolfi, F. Viola, F. Gallaire, and S. Camarri, Suppression of von Kármán vortex streets past porous rectangular cylinders, Physical Review Fluids **3**, 103901 (2018).

[22] T. Tang, J. Xie, S. Yu, J. Li, and P. Yu, Effect of aspect ratio on flow through and around a porous disk, Physical Review Fluids **6**, 074101 (2021).

[23] P. Yu, Y. Zeng, T. S. Lee, X. B. Chen, and H. T. Low, Numerical simulation on steady flow around and through a porous sphere, International Journal of Heat and Fluid Flow **36**, 142 (2012).

[24] M. Ciuti, G. A. Zampogna, F. Gallaire, S. Camarri, and P. G. Ledda, On the effect of a penetrating recirculation region on the bifurcations of the flow past a permeable sphere, Physics of Fluids **33**, 124103 (2021).

[25] P. Yu, Y. Zeng, T. S. Lee, X. B. Chen, and H. T. Low, Steady flow around and through a permeable circular cylinder, Computers and Fluids **42**, 1 (2011).

[26] C. Jackson, A finite-element study of the onset of vortex shedding in flow past variously shaped bodies, Journal of Fluid Mechanics **182**, 23 (1987).

[27] M. Provansal, C. Mathis, and L. Boyer, Bénard-von Kármán instability: transient and forced regimes, Journal of Fluid Mechanics **182**, 1 (1987).

[28] B. R. Noack, M. König, and H. Eckelmann, Three-dimensional stability analysis of the periodic flow around a circular cylinder, Physics of Fluids A: Fluid Dynamics **5**, 1279 (1993).

[29] B. R. Noack and H. Eckelmann, A global stability analysis of the steady and periodic cylinder wake, Journal of Fluid Mechanics **270**, 297 (1994).

[30] T. Leweke and C. H. Williamson, Three-dimensional instabilities in wake transition, European Journal of Mechanics-B/Fluids **17**, 571 (1998).

[31] C. Williamson, The existence of two stages in the transition to three-dimensionality of a cylinder wake, The Physics of fluids **31**, 3165 (1988).

[32] C. H. K. Williamson, Vortex dynamics in the cylinder wake, Annual Review of Fluid Mechanics **28**, 477 (1996).

[33] D. Barkley and R. D. Henderson, Three-dimensional Floquet stability analysis of the wake of a circular cylinder, J. Fluid Mech. **322**, 215 (1996).

[34] V. Theofilis, Global linear instability, Annual Review of Fluid Mechanics **43**, 319 (2011).

[35] C. H. K. Williamson, Vortex dynamics in the cylinder wake, Annual Review of Fluid Mechanics **28**, 477 (1996).

[36] C. Williamson, Three-dimensional wake transition, Journal of Fluid Mechanics **328**, 345 (1996).

[37] R. Pierrehumbert, Universal short-wave instability of two-dimensional eddies in an inviscid fluid, Physical review letters **57**, 2157 (1986).

[38] B. Bayly, Three-dimensional instability of elliptical flow, Physical review letters **57**, 2160 (1986).

[39] R. R. Kerswell, Elliptical instability, Annual review of fluid mechanics **34**, 83 (2002).

[40] C. Caulfield and R. Kerswell, The nonlinear development of three-dimensional disturbances at hyperbolic stagnation points: a model of the braid region in mixing layers, Physics of Fluids **12**, 1032 (2000).

[41] S. Julien, S. Ortiz, and J.-M. Chomaz, Secondary instability mechanisms in the wake of a flat plate, European Journal of Mechanics-B/Fluids **23**, 157 (2004).

[42] P. J. Schmid, Dynamic mode decomposition of numerical and experimental data, J. Fluid Mech. **656**, 5 (2010).

[43] P. J. Schmid, Application of the dynamic mode decomposition to experimental data, Experiments in Fluids **50**, 1123 (2011).

[44] M. R. Jovanović, P. J. Schmid, and J. W. NicholsW, Sparsity-promoting dynamic mode decomposition, Physics of Fluids **26**, 024103 (2014).

[45] T. Sayadi, P. J. Schmid, F. Richecoeur, and D. Durox, Parametrized data-driven decomposition for bifurcation analysis, with application to thermo-acoustically unstable systems, Physics of Fluids **27**, 037102 (2015).

[46] J. Kou and W. Zhang, An improved criterion to select dominant modes from dynamic mode decomposition, European Journal of Mechanics-B/Fluids **62**, 109 (2017).

[47] A. G. Nair, B. Strom, B. W. Brunton, and S. L. Brunton, Phase-consistent dynamic mode decomposition from multiple overlapping spatial domains, Physical Review Fluids **5**, 074702 (2020).

[48] W. Zhang and M. Wei, Generalized eigenvalue approach for dynamic mode decomposition, AIP Advances **11**, 125011 (2021).

[49] M. Icardi, G. Boccardo, D. Marchisio, T. Tosco, and R. Sethi, Pore-scale simulation of fluid flow and solute dispersion in three-dimensional porous media, Physical Review E **90**, 013032 (2014).

[50] J. Crabill, F. Witherden, and A. Jameson, A parallel direct cut algorithm for high-order overset methods with application to a spinning golf ball, Journal of Computational Physics **374**, 692 (2018).

[51] U. Hornung, *Homogenization and Porous Media*, edited by L. Kadanoff, J. E. Marsden, L. Sirovich, and S. Wiggins (Springer, New York, 1997).

[52] G. Zampogna and F. Gallaire, Effective stress jump across membranes, Journal of Fluid Mechanics **892**, A9 (2020).

[53] G. A. Zampogna, P. G. Ledda, and F. Gallaire, Transport across thin membranes: effective solute flux jump, Physics of Fluids **34**, 083113 (2022).

[54] G. A. Zampogna and A. Bottaro, Fluid flow over and through a regular bundle of rigid fibres, Journal of Fluid Mechanics **792**, 5 (2016).

[55] U. Lācis, G. A. Zampogna, and S. Bagheri, A computational continuum model of poroelastic beds, Proceedings of the Royal Society A: Mathematical, Physical and Engineering Sciences **473**, 20160932 (2017).

[56] G. Zampogna, U. Lācis, S. Bagheri, and A. Bottaro, Modeling waves in fluids flowing over and through poroelastic media, International Journal of Multiphase Flow **110**, 148 (2019).

[57] G. A. Zampogna, J. Magnaudet, and A. Bottaro, Generalized slip condition over rough surfaces, Journal of Fluid Mechanics **858**, 407–436 (2019).

[58] E. N. Ahmed, S. B. Naqvi, L. Buda, and A. Bottaro, A homogenization approach for turbulent channel flows over porous substrates: Formulation and implementation of effective boundary conditions, Fluids **7**, 178 (2022).

[59] E. N. Ahmed, A. Bottaro, and G. Tanda, A homogenization approach for buoyancy-induced flows over micro-textured vertical surfaces, Journal of Fluid Mechanics **941** (2022).

[60] U. Lācis and S. Bagheri, A framework for computing effective boundary conditions at the interface between free fluid and a porous medium, Journal of Fluid Mechanics **812**, 866 (2017).

[61] U. Lācis, Y. Sudhakar, S. Pasche, and S. Bagheri, Transfer of mass and momentum at rough and porous surfaces, Journal of Fluid Mechanics **884**, A21 (2020).

[62] A. Bottaro, Flow over natural or engineered surfaces: an adjoint homogenization perspective, Journal of Fluid Mechanics **877**, P1 (2019).

[63] U. Lācis, G. Zampogna, and S. Bagheri, A computational continuum model of poroelastic beds, Proceedings of the Royal Society A: Mathematical, Physical and Engineering Sciences **473**, 20160932 (2017).

[64] S. B. Naqvi and A. Bottaro, Interfacial conditions between a free-fluid region and a porous medium, International Journal of Multiphase Flow **141**, 103585 (2021).

[65] A. Quarteroni, Domain decomposition methods, in *Numerical Models for Differential Problems* (Springer International Publishing, Cham, 2017) pp. 555–612.

[66] G. S. Beavers and D. D. Joseph, Boundary conditions at a natural permeable wall, Journal of Fluid Mechanics **30**, 197 (1967).

[67] P. Meliga, J.-M. Chomaz, and D. Sipp, Unsteadiness in the wake of disks and spheres: instability, receptivity and control using direct and adjoint global stability analyses, J. Fluids. Struct. **25**, 601 (2009).

[68] P. A. Monkewitz and K. Sohn, Absolute instability in hot jets, AIAA journal **26**, 911 (1988).

[69] F. Giannetti and P. Luchini, Structural sensitivity of the first instability of the cylinder wake, Journal of Fluid Mechanics **581**, 167 (2007).

[70] B. Kumar and S. Mittal, On the origin of the secondary vortex street, Journal of Fluid Mechanics **711**, 641–666 (2012).

[71] P. Vorobieff, D. Georgiev, and M. S. Ingber, Onset of the second wake: Dependence on the Reynolds number, Physics of Fluids **14**, L53

(2002).

[72] J. Robichaux, S. Balachandar, and S. P. Vanka, Three-dimensional Floquet instability of the wake of square cylinder, Physics of Fluids **11**, 560 (1999).

[73] Dmdsp: Software for sparsity-promoting dynamic mode decomposition, `https://github.com/aaren/sparse_dmd/tree/master/matlab`, accessed: 2014-07-03.

[74] M. Landman and P. Saffman, The three-dimensional instability of strained vortices in a viscous fluid, The Physics of fluids **30**, 2339 (1987).

[75] E. de Langre, Effects of wind on plants, Annual Review of Fluid Mechanics **40**, 141 (2008).

[76] H. M. Nepf, Drag, turbulence, and diffusion in flow through emergent vegetation, Water Resources Research **35**, 479 (1999), https://agupubs.onlinelibrary.wiley.com/doi/pdf/10.1029/1998WR900069.

[77] T. Lu, H. Stone, and M. Ashby, Heat transfer in open-cell metal foams, Acta Materialia **46**, 3619 (1998).

[78] H. Wang, C. Peng, W. Li, C. Ding, T. Ming, and N. Zhou, Porous media: A faster numerical simulation method applicable to real urban communities, Urban Climate **38**, 100865 (2021).